

Updated Measurement of the Strong Phase in $D^0 \rightarrow K^+\pi^-$ Decay Using Quantum Correlations in $e^+e^- \rightarrow D^0\bar{D}^0$ at CLEO

D. M. Asner,¹ G. Tatishvili,¹ J. Y. Ge,² D. H. Miller,² I. P. J. Shipsey,² B. Xin,²
 G. S. Adams,³ J. Napolitano,³ K. M. Ecklund,⁴ Q. He,⁵ J. Insler,⁵ H. Muramatsu,⁵
 L. J. Pearson,⁵ E. H. Thorndike,⁵ M. Artuso,⁶ S. Blusk,⁶ N. Horwitz,⁶ R. Mountain,⁶
 T. Skwarnicki,⁶ S. Stone,⁶ J. C. Wang,⁶ L. M. Zhang,⁶ P. U. E. Onyisi,⁷ G. Bonvicini,⁸
 D. Cinabro,⁸ A. Lincoln,⁸ M. J. Smith,⁸ P. Zhou,⁸ P. Naik,⁹ J. Rademacker,⁹
 K. W. Edwards,¹⁰ E. J. White,^{10,*} R. A. Briere,¹¹ H. Vogel,¹¹ P. U. E. Onyisi,¹²
 J. L. Rosner,¹² J. P. Alexander,¹³ D. G. Cassel,¹³ S. Das,¹³ R. Ehrlich,¹³ L. Gibbons,¹³
 S. W. Gray,¹³ D. L. Hartill,¹³ D. L. Kreinick,¹³ V. E. Kuznetsov,¹³ J. R. Patterson,¹³
 D. Peterson,¹³ D. Riley,¹³ A. Ryd,¹³ A. J. Sadoff,¹³ X. Shi,^{13,†} S. Stroiney,¹³
 W. M. Sun,¹³ J. Yelton,¹⁴ P. Rubin,¹⁵ N. Lowrey,¹⁶ S. Mehrabyan,¹⁶ M. Selen,¹⁶
 J. Wiss,¹⁶ J. Libby,¹⁷ M. Kornicer,¹⁸ R. E. Mitchell,¹⁸ D. Besson,¹⁹ T. K. Pedlar,²⁰
 D. Cronin-Hennessy,²¹ J. Hietala,²¹ S. Dobbs,²² Z. Metreveli,²² K. K. Seth,²²
 A. Tomaradze,²² T. Xiao,²² A. Powell,²³ C. Thomas,²³ and G. Wilkinson²³

(CLEO Collaboration)

¹*Pacific Northwest National Laboratory, Richland, WA 99352, USA*

²*Purdue University, West Lafayette, Indiana 47907, USA*

³*Rensselaer Polytechnic Institute, Troy, New York 12180, USA*

⁴*Rice University, Houston, Texas 77005, USA*

⁵*University of Rochester, Rochester, New York 14627, USA*

⁶*Syracuse University, Syracuse, New York 13244, USA*

⁷*University of Texas at Austin, Austin, TX 78712*

⁸*Wayne State University, Detroit, Michigan 48202, USA*

⁹*University of Bristol, Bristol BS8 1TL, United Kingdom*

¹⁰*Carleton University, Ottawa, Ontario, Canada K1S 5B6*

¹¹*Carnegie Mellon University, Pittsburgh, Pennsylvania 15213, USA*

¹²*University of Chicago, Chicago, Illinois 60637, USA*

¹³*Cornell University, Ithaca, New York 14853, USA*

¹⁴*University of Florida, Gainesville, Florida 32611, USA*

¹⁵*George Mason University, Fairfax, Virginia 22030, USA*

¹⁶*University of Illinois, Urbana-Champaign, Illinois 61801, USA*

¹⁷*Indian Institute of Technology Madras,
Chennai, Tamil Nadu 600036, India*

¹⁸*Indiana University, Bloomington, Indiana 47405, USA*

¹⁹*University of Kansas, Lawrence, Kansas 66045, USA*

²⁰*Luther College, Decorah, Iowa 52101, USA*

²¹*University of Minnesota, Minneapolis, Minnesota 55455, USA*

²²*Northwestern University, Evanston, Illinois 60208, USA*

²³*University of Oxford, Oxford OX1 3RH, United Kingdom*

(Dated: October 2, 2012)

Abstract

We analyze a sample of 3 million quantum-correlated $D^0\bar{D}^0$ pairs from 818 pb⁻¹ of e^+e^- collision data collected with the CLEO-c detector at $E_{\text{cm}} = 3.77$ GeV, to give an updated measurement of $\cos\delta$ and a first determination of $\sin\delta$, where δ is the relative strong phase between doubly Cabibbo-suppressed $D^0 \rightarrow K^+\pi^-$ and Cabibbo-favored $\bar{D}^0 \rightarrow K^+\pi^-$ decay amplitudes. With no inputs from other experiments, we find $\cos\delta = 0.81_{-0.18-0.05}^{+0.22+0.07}$, $\sin\delta = -0.01 \pm 0.41 \pm 0.04$, and $|\delta| = (10_{-53-0}^{+28+13})^\circ$. By including external measurements of mixing parameters, we find alternative values of $\cos\delta = 1.15_{-0.17-0.08}^{+0.19+0.00}$, $\sin\delta = 0.56_{-0.31-0.20}^{+0.32+0.21}$, and $\delta = (18_{-17}^{+11})^\circ$. Our results can be used to improve the world average uncertainty on the mixing parameter y by approximately 10%.

* Now at: University of Cincinnati, Cincinnati, Ohio 45221

† Now at: National Taiwan University, Taipei, Taiwan

I. INTRODUCTION

Charm mixing in the Standard Model is conventionally described by two small dimensionless parameters:

$$x \equiv 2 \frac{M_2 - M_1}{\Gamma_2 + \Gamma_1} \quad (1)$$

$$y \equiv \frac{\Gamma_2 - \Gamma_1}{\Gamma_2 + \Gamma_1}, \quad (2)$$

where $M_{1,2}$ and $\Gamma_{1,2}$ are the masses and widths, respectively, of the neutral D meson CP eigenstates, D_1 (CP -odd) and D_2 (CP -even), defined by

$$|D_1\rangle \equiv \frac{|D^0\rangle + |\bar{D}^0\rangle}{\sqrt{2}} \quad (3)$$

$$|D_2\rangle \equiv \frac{|D^0\rangle - |\bar{D}^0\rangle}{\sqrt{2}}, \quad (4)$$

assuming CP conservation. The mixing probability is then denoted by $R_M \equiv (x^2 + y^2)/2$, and the width of the D^0 and \bar{D}^0 flavor eigenstates is $\Gamma \equiv (\Gamma_1 + \Gamma_2)/2$.

Recent experimental studies of charm mixing parameters have probed x and y directly [1–7], as well as the “rotated” parameter $y' \equiv y \cos \delta - x \sin \delta$ [8–10]. Here, $-\delta$ is the relative phase between the doubly Cabibbo-suppressed $D^0 \rightarrow K^+\pi^-$ amplitude and the corresponding Cabibbo-favored $\bar{D}^0 \rightarrow K^+\pi^-$ amplitude: $\langle K^+\pi^- | D^0 \rangle / \langle K^+\pi^- | \bar{D}^0 \rangle \equiv r e^{-i\delta}$. We adopt a convention in which δ corresponds to a strong phase, which vanishes in the SU(3) limit [11]. The magnitude r of the amplitude ratio is approximately 0.06. In this article, we update an analysis [12] that first directly determined $\cos \delta$ using correlated production of D^0 and \bar{D}^0 mesons in e^+e^- collisions produced at the Cornell Electron Storage Ring and collected with the CLEO-c detector. In the current analysis, we also present a first measurement of $\sin \delta$.

At the $\psi(3770)$ resonance, the $D^0\bar{D}^0$ pair is produced with no accompanying particles, so it is in a quantum-coherent $C = -1$ state. As a result, the $D^0\bar{D}^0$ decay rates differ from incoherent decay rates because of interference effects. These differences depend on y (to first order) and on strong phases of the decay amplitudes [11, 13–22]. As in our previous analysis, we implement the double-tagging method with a χ^2 fit described in Ref. [23], where, in addition to extracting the number of $D^0\bar{D}^0$ pairs produced (\mathcal{N}) and the branching fractions (\mathcal{B}) of the reconstructed D^0 final states, we simultaneously determine y , x^2 , r^2 , $\cos \delta$, and $\sin \delta$, all without needing to know the integrated luminosity or $D^0\bar{D}^0$ production cross section. The main improvements in the current analysis are: use of the full CLEO-c $\psi(3770)$ dataset (which is three times larger than the previous dataset), reconstruction of additional CP eigenstates, reconstruction of semimuonic D^0 decays, addition of modes that provide sensitivity to $\sin \delta$, and direct measurement of the amplitude ratio r .

As before, we neglect CP violation in D decays and mixing. Recently, evidence has been found [24–26] for direct CP violation in $D \rightarrow K^+K^-$ and $D \rightarrow \pi^+\pi^-$ decays, with CP asymmetries of $\mathcal{O}(10^{-2})$. The current analysis also uses $D \rightarrow K^+K^-$ and $D \rightarrow \pi^+\pi^-$ decays, and the above CP asymmetries would bias our determinations of $\cos \delta$ and $\sin \delta$ from these modes by $\mathcal{O}(10^{-2})$. By itself, this bias is much smaller than our experimental uncertainties, but its effect is further diluted by our use of additional CP eigenstates in the analysis. We are also insensitive to CP violation in mixing and in the interference between

mixing and decay at the levels currently allowed by experimental constraints [27]. These sources of CP violation would bias our measured value of y .

The paper is organized as follows. In Section II, we review the formalism of quantum-correlated $D^0\bar{D}^0$ decay. Section III describes the event selection criteria and D reconstruction procedures. The external measurements used in the fit are summarized in Section IV. Systematic uncertainties, which are also input to the fit, are discussed in Section V. Finally, we present and discuss our main fit results in Section VI.

II. FORMALISM AND PHENOMENOLOGY

For decays of isolated D^0 mesons, we define the following quantities for each final state i :

$$r_i^2 \equiv \frac{\int \bar{A}_i(\mathbf{x})\bar{A}_i^*(\mathbf{x})d\mathbf{x}}{\int A_i(\mathbf{x})A_i^*(\mathbf{x})d\mathbf{x}} \quad (5)$$

$$R_i e^{-i\delta_i} \equiv \frac{\int \bar{A}_i(\mathbf{x})A_i^*(\mathbf{x})d\mathbf{x}}{r_i A_i^2} \quad (6)$$

where $A_i \equiv \langle i|D^0\rangle$ and $\bar{A}_i \equiv \langle i|\bar{D}^0\rangle$, and the integral is over the phase space for mode i . Thus, δ_i is an average phase for the final state i , and $R_i \in [0, 1]$ is a coherence factor [28] that characterizes the variation of δ_i over phase space. If the final state is two-body, like $K^-\pi^+$, then it occupies a single phase space point, and $R = 1$.

For a $D^0\bar{D}^0$ pair produced through the $\psi(3770)$ resonance, the decay rate to an exclusive final state $\{i, j\}$, where i and j label the final states of the two D mesons, follows from the antisymmetric amplitude \mathcal{M}_{ij} :

$$\begin{aligned} \Gamma(i, j) \propto \mathcal{M}_{ij}^2 &= |A_i\bar{A}_j - \bar{A}_i A_j|^2 \\ &= |\langle i|D_2\rangle\langle j|D_1\rangle - \langle i|D_1\rangle\langle j|D_2\rangle|^2 + \mathcal{O}(x^2, y^2), \end{aligned} \quad (7)$$

where the $\mathcal{O}(x^2, y^2)$ term represents a mixed amplitude. The interference between mixed and unmixed amplitudes vanishes when integrated over time because it depends on the difference between the D^0 and \bar{D}^0 decay times. If we denote the charge conjugates of modes i and j by \bar{i} and \bar{j} , then Equation (7) leads to the following expressions in terms of the parameters defined above:

$$\Gamma(i, \bar{j}) = \Gamma(\bar{i}, j) \propto A_i^2 A_j^2 \left(1 + r_i^2 r_j^2 - 2r_i R_i \cos \delta_i r_j R_j \cos \delta_j - 2r_i R_i \sin \delta_i r_j R_j \sin \delta_j \right) \quad (8)$$

$$\Gamma(i, j) = \Gamma(\bar{i}, \bar{j}) \propto A_i^2 A_j^2 \left(r_i^2 + r_j^2 - 2r_i R_i \cos \delta_i r_j R_j \cos \delta_j + 2r_i R_i \sin \delta_i r_j R_j \sin \delta_j \right), \quad (9)$$

where the latter rate is reduced by half if i and j are identical. Experimentally, these rates correspond to yields of double tags (DT), which are events where both D^0 and \bar{D}^0 are reconstructed.

The above amplitudes are normalized to the uncorrelated branching fractions \mathcal{B}_i :

$$\mathcal{B}_i \equiv \mathcal{B}(D^0 \rightarrow i) = A_i^2 [1 + r_i R_i (y \cos \delta_i + x \sin \delta_i)] \quad (10)$$

$$\mathcal{B}_{\bar{i}} \equiv \mathcal{B}(\bar{D}^0 \rightarrow i) = A_i^2 [r_i^2 + r_i R_i (y \cos \delta_i - x \sin \delta_i)]. \quad (11)$$

These \mathcal{B}_i are related to rates of single tags (ST), or individually reconstructed D^0 or \bar{D}^0 candidates, which are obtained by summing over DT rates:

$$\Gamma(i, X) = \sum_j [\Gamma(i, j) + \Gamma(i, \bar{j})] = \mathcal{B}_i + \mathcal{B}_{\bar{i}} = A_i^2 (1 + 2y r_i R_i \cos \delta_i + r_i^2). \quad (12)$$

Here, we have used an expression for y in terms of r_i , R_i , and δ_i , which is derived from Eqs. (2–4) and Eqs. (5–6):

$$y = \frac{\sum_i \left[\int |A_i(\mathbf{x}) - \bar{A}_i(\mathbf{x})|^2 d\mathbf{x} - \int |A_i(\mathbf{x}) + \bar{A}_i(\mathbf{x})|^2 d\mathbf{x} \right]}{\sum_i \left[\int |A_i(\mathbf{x}) - \bar{A}_i(\mathbf{x})|^2 d\mathbf{x} + \int |A_i(\mathbf{x}) + \bar{A}_i(\mathbf{x})|^2 d\mathbf{x} \right]} = -2 \frac{\sum_i A_i^2 r_i R_i \cos \delta_i}{\sum_i A_i^2 (1 + r_i^2)}. \quad (13)$$

Thus, both ST rates and the total rate, $\Gamma_{D^0 \bar{D}^0}$, are unaffected by quantum correlations between the D^0 and \bar{D}^0 decays, and our sensitivity to mixing comes from comparing ST to DT rates.

Table I gives the notation for the various r_i and δ_i that appear in this analysis. The final states of mixed CP (denoted by f and \bar{f} below) that we consider are $K^\mp \pi^\pm$ and $K_S^0 \pi^+ \pi^-$. Following Ref. [29], the $K_S^0 \pi^+ \pi^-$ Dalitz plot is divided into eight bins according to the strong phase of the decay amplitude. We denote the portions of $K_S^0 \pi^+ \pi^-$ in phase bin i by Y_i and \bar{Y}_i , where $m_{K_S^0 \pi^-} < m_{K_S^0 \pi^+}$ for Y_i , and $m_{K_S^0 \pi^-} > m_{K_S^0 \pi^+}$ for \bar{Y}_i . The corresponding amplitude ratio magnitudes and branching fraction ratios integrated over bin i are denoted by ρ_i and Q_i , respectively. As in Ref. [29], we denote the real and imaginary parts of Eq. (6) by c_i and s_i , respectively, but with the opposite sign convention for s_i . Semileptonic final states (ℓ^\pm), CP -even eigenstates (S_+), and CP -odd eigenstates (S_-) have known values of r_i and δ_i , which give them unique leverage in determining the parameters in the other final states, as demonstrated below. Note that, as shown in Eqs. (10) and (11), the ratio $\mathcal{B}_i/\mathcal{B}_i$ does not equal r_i^2 in general.

TABLE I. Parameters describing the ratio of amplitudes A_i and \bar{A}_i for the final states i . The \cdot indicates that we do not make explicit reference to δ_i for the Y_k modes in this article, but consider only c_k and s_k instead.

Final State	r_i	δ_i	$R_i \cos \delta_i$	$R_i \sin \delta_i$	$\mathcal{B}_i/\mathcal{B}_i$
$K^\mp \pi^\pm$	r	δ	$\cos \delta$	$\sin \delta$	R_{WS}
Y_k/\bar{Y}_k	ρ_k	\cdot	c_k	s_k	Q_k
S_+	1	π	-1	0	1
S_-	1	0	+1	0	1
ℓ^\pm	0	—	—	—	0

Using the definitions in Table I, we evaluate in Table II the quantum-correlated $D^0 \bar{D}^0$ branching fractions, \mathcal{F}^{cor} , for all categories of final states reconstructed in this analysis; we also give the corresponding uncorrelated branching fractions, \mathcal{F}^{unc} . Comparing \mathcal{F}^{cor} with \mathcal{F}^{unc} allows us to extract y , r^2 , $\cos \delta$, and $\sin \delta$. Although we neglect x^2 and y^2 terms in general, we report a result for x^2 as determined solely from the suppressed $\{K^\pm \pi^\mp, K^\pm \pi^\mp\}$ final states.

From Table II, one finds that, given r^2 and y , $\cos \delta$ can be determined by measuring the size of the interference between $K^- \pi^+$ and a CP eigenstate. The CP of the eigenstate tags the $K^- \pi^+$ parent D to be a CP eigenstate with the opposite eigenvalue. Since this D eigenstate is a linear combination of the flavor eigenstates D^0 and \bar{D}^0 , the decay rate is modulated by the relative phase between the $D^0 \rightarrow K^- \pi^+$ and $\bar{D}^0 \rightarrow K^- \pi^+$ amplitudes.

Similarly, probing $\sin \delta$ requires the interference of $K^- \pi^+$ with another mode, such as $K_S^0 \pi^+ \pi^-$, that has non-zero $R_i \sin \delta_i$. However, unlike CP eigenstates, the phases in $K_S^0 \pi^+ \pi^-$

TABLE II. Correlated (C -odd) and uncorrelated effective $D^0\bar{D}^0$ branching fractions, \mathcal{F}^{cor} and \mathcal{F}^{unc} , to leading order in x , y and R_{WS} , divided by \mathcal{B}_i for ST modes i and $\mathcal{B}_i\mathcal{B}_j$ for DT modes $\{i, j\}$. Charge conjugate modes are implied.

Mode	Correlated	Uncorrelated
$K^-\pi^+$	$1 + R_{\text{WS}}$	$1 + R_{\text{WS}}$
S_+	2	2
S_-	2	2
Y_k	$1 + Q_k$	$1 + Q_k$
$K^-\pi^+, K^-\pi^+$	$R_{\text{M}}[(1 + R_{\text{WS}})^2 - 4r \cos \delta(r \cos \delta + y)]$	R_{WS}
$K^-\pi^+, K^+\pi^-$	$(1 + R_{\text{WS}})^2 - 4r \cos \delta(r \cos \delta + y)$	$1 + R_{\text{WS}}^2$
$K^-\pi^+, S_+$	$1 + R_{\text{WS}} + 2r \cos \delta + y$	$1 + R_{\text{WS}}$
$K^-\pi^+, S_-$	$1 + R_{\text{WS}} - 2r \cos \delta - y$	$1 + R_{\text{WS}}$
$K^-\pi^+, \ell^-$	$1 - ry \cos \delta - rx \sin \delta$	1
$K^-\pi^+, \ell^+$	$r^2(1 - ry \cos \delta - rx \sin \delta)$	R_{WS}
$K^-\pi^+, \bar{Y}_i$	$(1 + R_{\text{WS}})(1 + Q_i) - r^2 - \rho_i^2$ $-2(r \cos \delta + y)(\rho_i c_i + y) + 2r \sin \delta \rho_i s_i$	$1 + R_{\text{WS}}Q_i$
$K^-\pi^+, Y_i$	$(1 + R_{\text{WS}})(1 + Q_i) - 1 - r^2 \rho_i^2$ $-2(r \cos \delta + y)(\rho_i c_i + y) - 2r \sin \delta \rho_i s_i$	$R_{\text{WS}} + Q_i$
S_+, S_+	0	1
S_-, S_-	0	1
S_+, S_-	4	2
S_+, ℓ^-	$1 + y$	1
S_-, ℓ^-	$1 - y$	1
S_+, Y_i	$1 + Q_i + 2\rho_i c_i + y$	$1 + Q_i$
S_-, Y_i	$1 + Q_i - 2\rho_i c_i - y$	$1 + Q_i$
Y_i, ℓ^-	$1 - \rho_i y c_i - \rho_i x s_i$	1
Y_i, ℓ^+	$\rho_i^2(1 - \rho_i y c_i - \rho_i x s_i)$	Q_i
Y_i, \bar{Y}_j	$(1 + Q_i)(1 + Q_j) - \rho_i^2 - \rho_j^2$ $-2(\rho_i c_i + y)(\rho_j c_j + y) + 2\rho_i s_i \rho_j s_j$	$1 + Q_i Q_j$
Y_i, Y_j	$(1 + Q_i)(1 + Q_j) - 1 - \rho_i^2 \rho_j^2$ $-2(\rho_i c_i + y)(\rho_j c_j + y) - 2\rho_i s_i \rho_j s_j$	$Q_i + Q_j$

are not fixed by a fundamental symmetry, so we must measure $\sin \delta$ and s_i simultaneously. Since these sine factors only appear in products with other sine factors, there is an overall sign ambiguity, which can be resolved by combining our measurements of $\sin \delta$ and $\cos \delta$ with external measurements of y' and x .

Our main source of information on y comes from CP -tagged semileptonic decays. In these weak transitions, the semileptonic decay width is independent of the parent D meson's CP eigenvalue. In contrast, the total width of the parent meson reflects its CP eigenvalue: $\Gamma_{1,2} = \Gamma(1 \mp y)$, so the semileptonic branching fraction for D_1 or D_2 is modified by a factor of $1 \pm y$. Thus, we determine y using exclusive final states $\{S_{\pm}, \ell\}$, where the S_{\pm} identifies the CP eigenvalue of the semileptonic decay's parent D . In this case, summing ℓ^+ and ℓ^- rates gives $\mathcal{F}_{S_{\pm}, \ell}^{\text{cor}} \approx 2\mathcal{B}_{S_{\pm}}\mathcal{B}_{\ell}(1 \pm y)$.

For r^2 , we use the fact that, because of the vanishing interference between mixed and

unmixed amplitudes, a DT with a semileptonic $K\ell\nu_\ell$ decay probes the bare matrix element squared, not the branching fraction, of the partner D . Therefore, we determine r^2 directly from $\{K\pi, K\ell\nu_\ell\}$ DT modes by taking the yield ratio for combinations with same-sign kaons and opposite-sign kaons.

III. EVENT SELECTION AND RECONSTRUCTION

Our current analysis is based on the full CLEO-c $\psi(3770)$ dataset with an integrated luminosity of 818 pb^{-1} , collected with the CLEO-c detector, which is described in Refs. [30–34]. We estimate signal efficiencies, background contributions, and probabilities for misreconstructing a produced signal decay in a different signal mode (crossfeed) using a GEANT-based [35] Monte Carlo simulated sample of uncorrelated $D^0\bar{D}^0$ decays with an effective integrated luminosity 20 times larger than that of our data sample. We reconstruct the final states shown in Table III, with $\pi^0 \rightarrow \gamma\gamma$, $\eta \rightarrow \gamma\gamma$, $K_S^0 \rightarrow \pi^+\pi^-$, and $\omega \rightarrow \pi^+\pi^-\pi^0$. Final states without K_L^0 mesons and neutrinos are fully reconstructed. For modes with K_L^0 mesons and neutrinos, which generally do not interact with the detector, we use a partial reconstruction technique, inferring the presence of the undetected particle via conservation of energy and momentum. In specifying the CP eigenvalue of a final state, we neglect CP violation in K^0 decays.

TABLE III. D final states reconstructed in this analysis.

Type	Reconstruction	Final States
f	full	$K^-\pi^+, Y_0 - Y_7$
\bar{f}	full	$K^+\pi^-, \bar{Y}_0 - \bar{Y}_7$
S_+	full	$K^+K^-, \pi^+\pi^-, K_S^0\pi^0\pi^0$
S_+	partial	$K_L^0\pi^0, K_L^0\eta, K_L^0\omega$
S_-	full	$K_S^0\pi^0, K_S^0\eta, K_S^0\omega$
S_-	partial	$K_L^0\pi^0\pi^0$
ℓ^+	partial	$K^-e^+\nu_e, K^-\mu^+\nu_\mu$
ℓ^-	partial	$K^+e^-\bar{\nu}_e, K^+\mu^-\bar{\nu}_\mu$

Final states that are common to those used in Ref. [12] are reconstructed with the same methods and selection criteria, except where noted below. In particular, the selection of π^\pm , K^\pm , and K_S^0 candidates remains unchanged. For π^0 and η candidates, we loosen the shower shape requirements to improve the agreement between efficiencies in data and those in simulated events. For all modes with ω candidates, we now apply a sideband subtraction in the $M(\pi^+\pi^-\pi^0)$ spectrum. Figure 1 shows the invariant mass distribution of ω candidates, along with the signal region of $760.0 \text{ MeV}/c^2 < M(\pi^+\pi^-\pi^0) < 805.0 \text{ MeV}/c^2$ and sideband regions of $600.0 \text{ MeV}/c^2 < M(\pi^+\pi^-\pi^0) < 730.0 \text{ MeV}/c^2$ and $830.0 \text{ MeV}/c^2 < M(\pi^+\pi^-\pi^0) < 852.5 \text{ MeV}/c^2$. The limited range of the upper sideband is chosen to minimize the effect of $\rho^0 \rightarrow \pi^+\pi^-$ and $\rho^\pm \rightarrow \pi^\pm\pi^0$ decays, which alter the shape of the background for $M(\pi^+\pi^-\pi^0)$ greater than approximately $870 \text{ MeV}/c^2$. The sidebands are scaled by a factor determined by fitting the $M(\pi^+\pi^-\pi^0)$ distribution in simulated events to a signal Gaussian plus a polynomial background and integrating the fitted background function. This sideband subtraction eliminates peaking backgrounds, which accounted for 5 – 10% of the observed

ω yields in Ref. [12]. We also make use of $K_S^0\pi^+\pi^-$ DT yields, efficiencies, and background estimates from Ref. [29], for the subset of modes in that analysis without $K_L^0\pi^+\pi^-$, $K^-\pi^+\pi^0$, or $K^-\pi^+\pi^-\pi^+$.

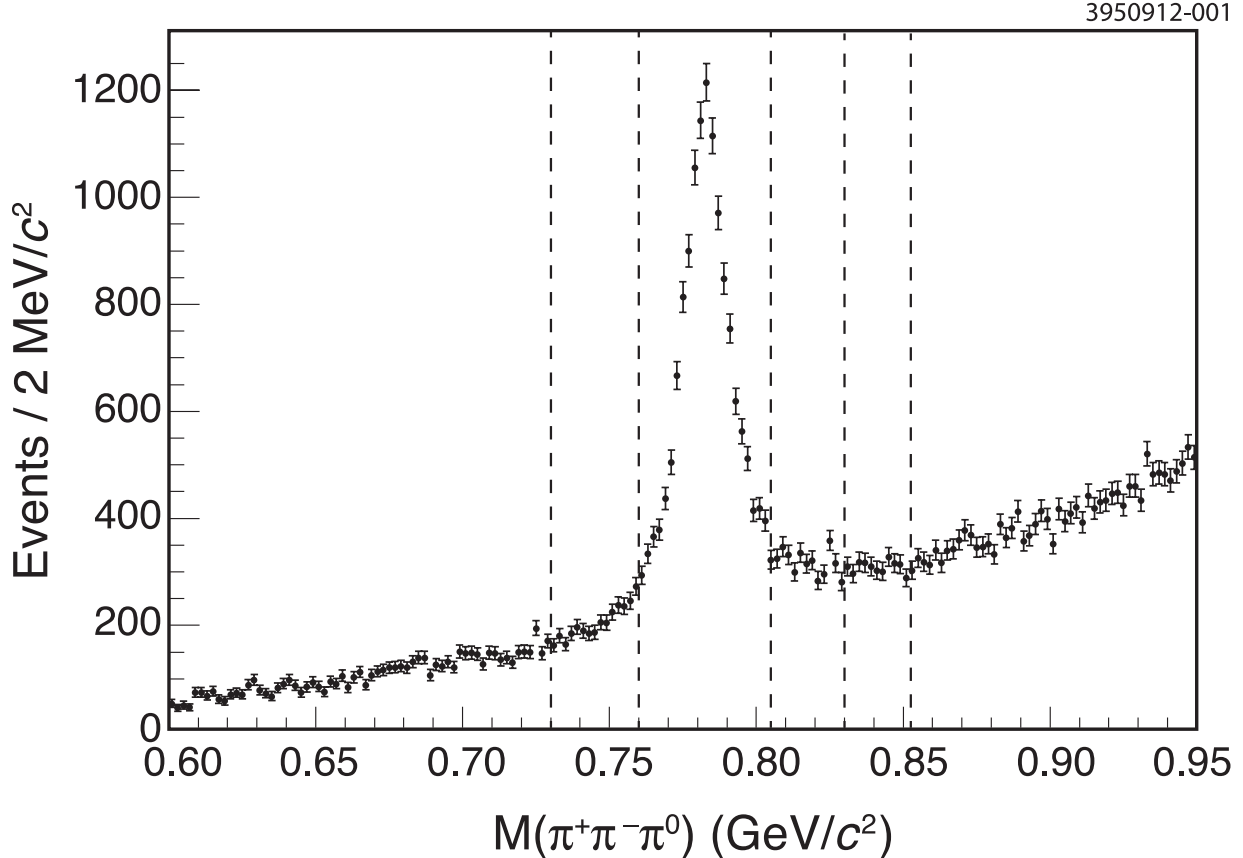


FIG. 1. Distribution of $M(\pi^+\pi^-\pi^0)$ for ω candidates. Data are shown as points with error bars, and the dashed lines mark the boundaries of the signal and sideband regions. As indicated in the text, the lower sideband ends at the lower limit of the graph.

A. Single Tags

We reconstruct ST candidates for the 8 modes in Table IV, utilizing the technique described in Ref. [12]. We do not include ST yields for $K_S^0\pi^+\pi^-$. As before, we identify ST candidates using two kinematic variables: the beam-constrained candidate mass M and the energy difference ΔE , which are defined to be

$$M \equiv \sqrt{E_D^2/c^4 - \mathbf{p}_D^2/c^2} \quad (14)$$

$$\Delta E \equiv E_D - E_0, \quad (15)$$

where \mathbf{p}_D and E_D are the total momentum and energy of the D candidate, and E_0 is the beam energy. After applying the mode-dependent requirements on ΔE listed in Table IV, we determine the ST yields by fitting the M distributions, shown in Fig. 2, to a signal shape derived from simulated signal events and to a background ARGUS function [36].

TABLE IV. Requirements on ΔE for ST D candidates.

Mode	Requirement (GeV)
$K^- \pi^+$	$ \Delta E < 0.0294$
$K^+ \pi^-$	$ \Delta E < 0.0294$
$K^+ K^-$	$ \Delta E < 0.0200$
$\pi^+ \pi^-$	$ \Delta E < 0.0300$
$K_S^0 \pi^0 \pi^0$	$-0.0550 < \Delta E < 0.0450$
$K_S^0 \pi^0$	$-0.0710 < \Delta E < 0.0450$
$K_S^0 \eta$	$-0.0550 < \Delta E < 0.0350$
$K_S^0 \omega$	$ \Delta E < 0.0250$

The measured ST yields and efficiencies are given in Table V. All efficiencies in this article include constituent branching fractions. The yield uncertainties are statistical and uncorrelated systematic, respectively. The latter arise from modeling of multiple candidates in simulation and variations in the signal lineshape. Correlated systematic uncertainties are discussed separately in Section V.

TABLE V. ST yields and efficiencies including constituent branching fractions. Yield uncertainties are statistical and uncorrelated systematic, respectively, and efficiency uncertainties are statistical only.

Mode	Yield	Efficiency (%)
$K^- \pi^+$	$75472 \pm 300 \pm 26$	63.74 ± 0.03
$K^+ \pi^-$	$75655 \pm 299 \pm 26$	64.76 ± 0.03
$K^+ K^-$	$13813 \pm 134 \pm 5$	56.15 ± 0.07
$\pi^+ \pi^-$	$6158 \pm 114 \pm 9$	72.08 ± 0.11
$K_S^0 \pi^0 \pi^0$	$9209 \pm 172 \pm 16$	14.34 ± 0.04
$K_S^0 \pi^0$	$23025 \pm 174 \pm 17$	31.53 ± 0.04
$K_S^0 \eta$	$3251 \pm 81 \pm 17$	10.81 ± 0.05
$K_S^0 \omega$	$9292 \pm 105 \pm 7$	12.89 ± 0.03

B. Fully Reconstructed Hadronic Double Tags

We reconstruct two categories of DT final states: 24 CP -allowed combinations of the 8 ST modes, and 136 modes with $K_S^0 \pi^+ \pi^-$. The second category includes 64 measurements where Y_i and \bar{Y}_i are paired with each of the eight ST modes [the sum of $\{K^- \pi^+, \bar{Y}_i\}$ and $\{K^+ \pi^-, Y_i\}$ (Cabibbo-favored), the sum of $\{K^- \pi^+, Y_i\}$ and $\{K^+ \pi^-, \bar{Y}_i\}$ (Cabibbo-suppressed), and the sum of Y_i and \bar{Y}_i paired with the six fully-reconstructed CP eigenstates], as well as 36 Cabibbo-favored combinations $\{Y_i, \bar{Y}_j\} + \{\bar{Y}_i, Y_j\}$, and 36 Cabibbo-suppressed combinations $\{Y_i, Y_j\} + \{\bar{Y}_i, \bar{Y}_j\}$. The 24 DT modes in the first category above were also used in Ref. [12], and we apply the same candidate selection criteria and yield determination methods as before, with the addition of the ω mass sideband subtraction discussed above. Figure 3 shows some representative two-dimensional M distributions. Event counts in the signal regions (S)

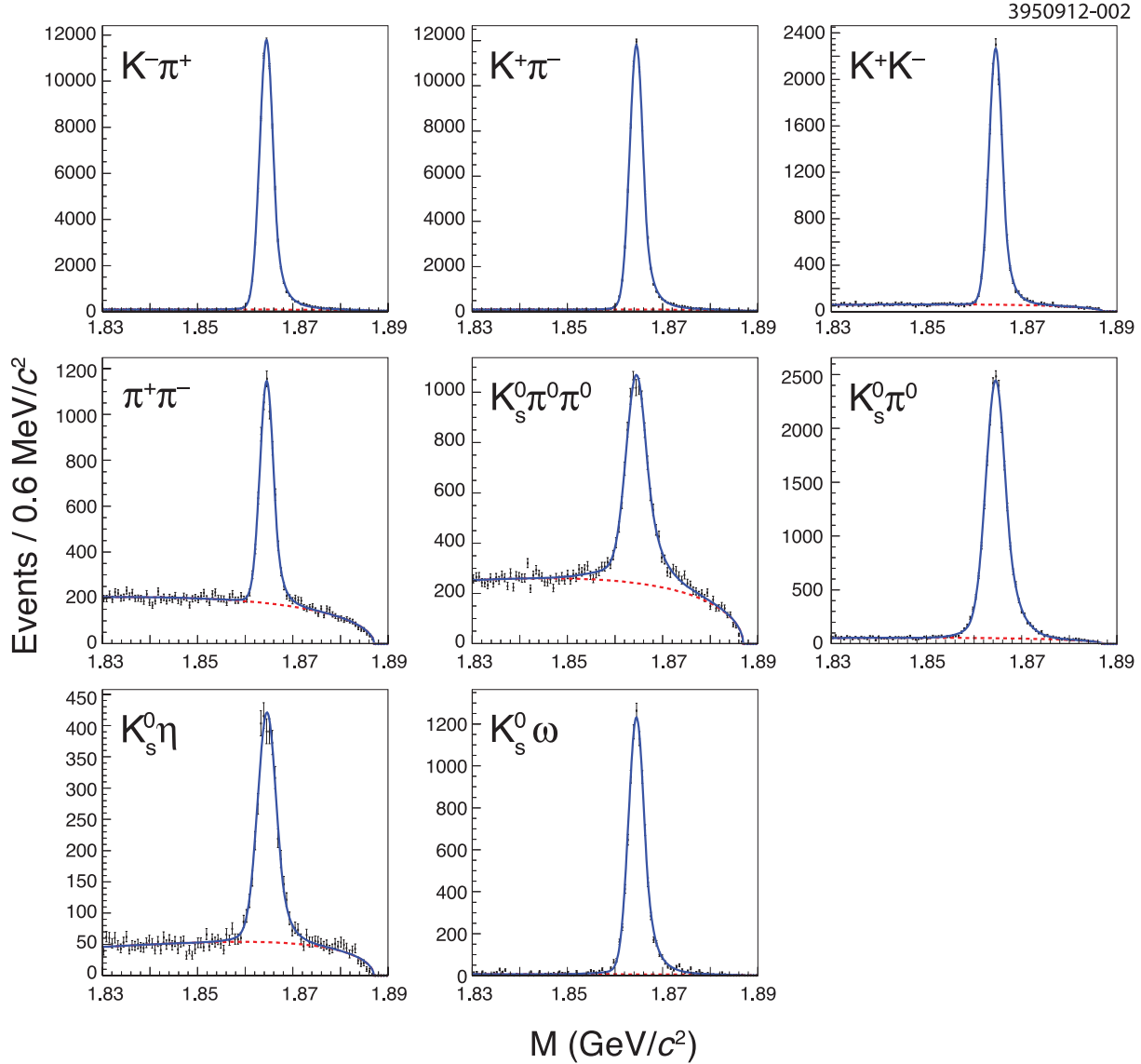


FIG. 2. ST M distributions and fits. Data are shown as points with error bars. The solid lines show the total fits, and the dashed lines show the background components.

are corrected by background estimates from the sideband regions (A, B, C, D), with sideband scaling factors determined by fitting the ST distributions in simulated events in the same manner as Section III A and integrating the fitted background function. Table VI gives the fully reconstructed DT yields and efficiencies for modes without $K_S^0 \pi^+ \pi^-$. To account for systematic effects in the sideband definitions and in the extrapolation to the signal regions, we assign a 100% systematic uncertainty on the size of the sideband subtractions, which is much smaller than the statistical uncertainties in all cases.

For DT modes with $K_S^0 \pi^+ \pi^-$, we use the signal yields, efficiencies, and background estimates determined in Ref. [29].

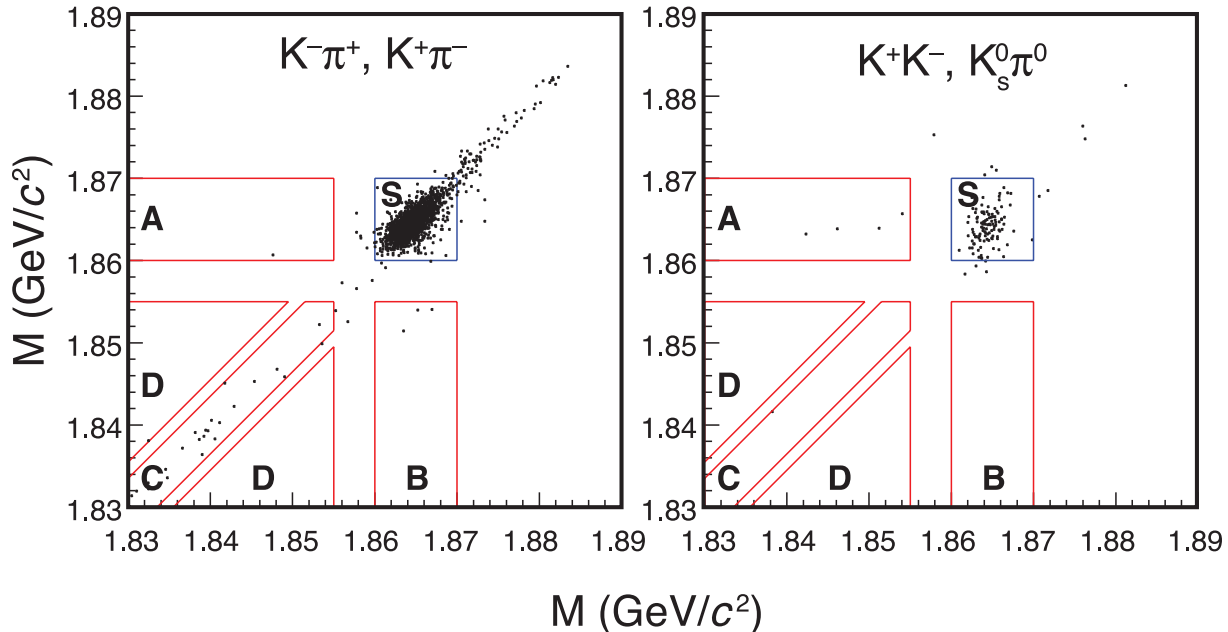


FIG. 3. Two-dimensional M distributions with signal (S) and sideband (A, B, C, D) regions depicted, for $\{K^-\pi^+, K^+\pi^-\}$ and $\{K^+K^-, K_S^0\pi^0\}$.

C. Double Tags with K_L^0

For hadronic DT modes with a single K_L^0 , we employ the same partial reconstruction technique as for $K_L^0\pi^0$ decays in Ref. [12], where the K_L^0 is identified by the four-vector recoiling against all other observed particles in the event. In the current analysis, we tag $K_L^0\pi^0$, $K_L^0\eta$, $K_L^0\omega$, and $K_L^0\pi^0\pi^0$ decays with fully reconstructed ST candidates, as allowed by CP conservation and selected as described in Section III A, and with an additional requirement of $1.86 \text{ GeV}/c^2 < M < 1.87 \text{ GeV}/c^2$. Each ST candidate is combined with a π^0 , η , ω candidate, or a pair of π^0 candidates. The signal process with K_L^0 appears as a peak in the squared recoil mass, M_{miss}^2 , against this system. As in Ref. [12], we suppress the background by vetoing events with additional unassigned charged particles, but we veto additional π^0 candidates only for the $K_L^0\eta$ mode. In addition, for all K_L^0 modes, we follow Ref. [29] by applying a veto on extra showers outside an energy-dependent cone around the predicted K_L^0 direction.

Figure 4 shows examples of the resultant M_{miss}^2 distributions in data. We obtain yields from event counts in the signal and sideband regions as shown in Table VII, where the sideband is scaled by a factor determined from simulated events. We also subtract a small contribution due to continuum $q\bar{q}$ production, which is also estimated from simulated events.

Table VIII lists the DT yields and efficiencies for K_L^0 modes without $K_S^0\pi^+\pi^-$. There are no uncorrelated systematic uncertainties for these modes. In the fit, we also include the $\{K_S^0\pi^+\pi^-, K_L^0\pi^0\}$ measurements from Ref. [29], which uses the same technique and criteria for $K_L^0\pi^0$ as those described above.

TABLE VI. Fully reconstructed DT yields and efficiencies including constituent branching fractions, for modes without $K_S^0\pi^+\pi^-$. Yield uncertainties are statistical and uncorrelated systematic, respectively, and efficiency uncertainties are statistical only.

Mode	Yield	Efficiency (%)
$K^-\pi^+, K^-\pi^+$	$5.6 \pm 2.5 \pm 0.4$	41.5 ± 2.8
$K^-\pi^+, K^+\pi^-$	$1731 \pm 42 \pm 11$	40.0 ± 0.2
$K^-\pi^+, K^+K^-$	$202 \pm 14 \pm 4$	35.2 ± 0.5
$K^-\pi^+, \pi^+\pi^-$	$82.6 \pm 9.1 \pm 0.4$	44.5 ± 0.9
$K^-\pi^+, K_S^0\pi^0\pi^0$	$132 \pm 12 \pm 1$	8.6 ± 0.2
$K^-\pi^+, K_S^0\pi^0$	$252 \pm 16 \pm 1$	19.4 ± 0.3
$K^-\pi^+, K_S^0\eta$	$36.7 \pm 6.2 \pm 1.3$	6.9 ± 0.3
$K^-\pi^+, K_S^0\omega$	$109 \pm 11 \pm 1$	8.5 ± 0.2
$K^+\pi^-, K^+\pi^-$	$4.0 \pm 2.0 \pm 0.0$	42.9 ± 2.9
$K^+\pi^-, K^+K^-$	$191 \pm 14 \pm 1$	35.3 ± 0.5
$K^+\pi^-, \pi^+\pi^-$	$77.3 \pm 8.9 \pm 0.7$	45.6 ± 0.9
$K^+\pi^-, K_S^0\pi^0\pi^0$	$121 \pm 11 \pm 2$	9.1 ± 0.2
$K^+\pi^-, K_S^0\pi^0$	$242 \pm 16 \pm 0$	20.0 ± 0.3
$K^+\pi^-, K_S^0\eta$	$35.2 \pm 6.0 \pm 0.8$	6.9 ± 0.3
$K^+\pi^-, K_S^0\omega$	$89.4 \pm 10.2 \pm 1.3$	8.7 ± 0.2
$K^+K^-, K_S^0\pi^0$	$107 \pm 11 \pm 2$	18.1 ± 0.5
$K^+K^-, K_S^0\eta$	$24.6 \pm 5.0 \pm 0.4$	5.6 ± 0.6
$K^+K^-, K_S^0\omega$	$47.6 \pm 7.2 \pm 0.0$	7.2 ± 0.4
$\pi^+\pi^-, K_S^0\pi^0$	$37.0 \pm 6.1 \pm 0.0$	21.3 ± 0.9
$\pi^+\pi^-, K_S^0\eta$	$6.0 \pm 2.5 \pm 0.0$	6.6 ± 1.0
$\pi^+\pi^-, K_S^0\omega$	$19.0 \pm 4.7 \pm 0.0$	9.4 ± 0.7
$K_S^0\pi^0\pi^0, K_S^0\pi^0$	$53.0 \pm 7.3 \pm 0.0$	4.1 ± 0.2
$K_S^0\pi^0\pi^0, K_S^0\eta$	$10.0 \pm 3.2 \pm 0.0$	1.4 ± 0.2
$K_S^0\pi^0\pi^0, K_S^0\omega$	$18.0 \pm 4.8 \pm 1.0$	1.5 ± 0.1

TABLE VII. Signal and sideband regions in M_{miss}^2 (GeV^2/c^4) for K_L^0 modes.

Mode	Signal Region	Sideband Region
$K_L^0\pi^0$	[0.10, 0.50]	[0.80, 2.00]
$K_L^0\eta$	[0.10, 0.45]	[0.75, 1.75]
$K_L^0\omega$	[0.15, 0.40]	[0.70, 1.25]
$K_L^0\pi^0\pi^0$	[0.10, 0.50]	[0.80, 1.80]

D. Semileptonic Double Tags

This Section describes our reconstruction of semileptonic D decays paired with fully reconstructed hadronic tags. In Section III E below, we discuss an additional semileptonic mode with two undetected particles.

In our previous analysis of Ref. [12], we reconstructed semielectronic final states inclu-

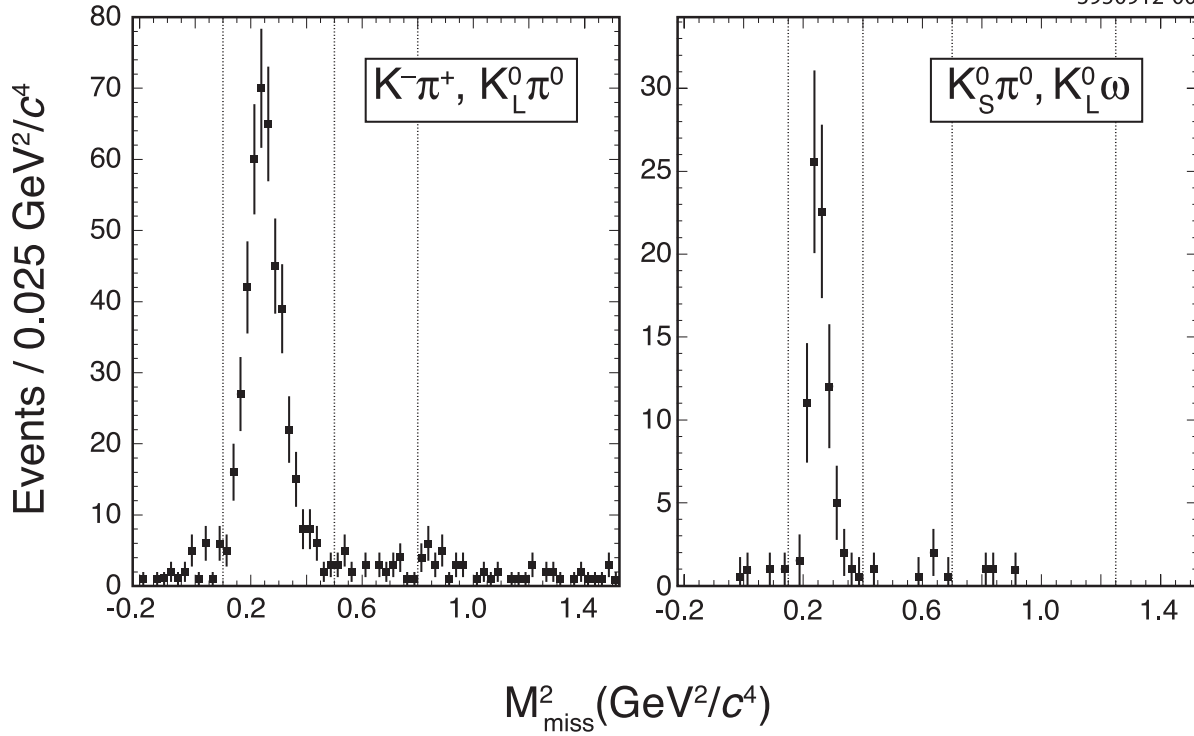


FIG. 4. Distributions of M_{miss}^2 for $\{K^-\pi^+, K_L^0\pi^0\}$ and $\{K_S^0\pi^0, K_L^0\omega\}$. The dashed lines show the signal and sideband regions. As indicated in Table VII, the sideband for $\{K^-\pi^+, K_L^0\pi^0\}$ extends beyond the upper limit of the graph.

sively, by identifying only the electron and not the accompanying neutrino or hadronic system. Also, we did not reconstruct semimuonic D^0 decays in Ref. [12]. In the current analysis, we replace inclusive reconstruction by exclusive reconstruction of $K^-e^+\nu_e$ and $K^+e^-\bar{\nu}_e$, which allows us, in general, to reduce systematic uncertainties because of lower background while keeping roughly the same statistical power. We also reconstruct $K^-\mu^+\nu_\mu$ and $K^+\mu^-\bar{\nu}_\mu$ without using the CLEO muon chambers because they are insensitive to muons in the momentum range of interest ($p_\mu < 1$ GeV/c). For both $Ke\nu_e$ and $K\mu\nu_\mu$, we begin with a fully reconstructed hadronic ST candidate, selected as described in Section III A, with additional requirements on M given in Secs. III D 1 and III D 2 below. Each ST candidate is then combined with a kaon and lepton candidate with opposite charges. To extract the signal yields, we calculate the quantity $U \equiv E_{\text{miss}} - cp_{\text{miss}}$, where E_{miss} and p_{miss} are the missing energy and the magnitude of the missing momentum, respectively, recoiling against the observed signal candidate particles in each event. Signal events peak at $U = 0$ GeV because of the undetected neutrino. Representative U distributions for $Ke\nu_e$ and $K\mu\nu_\mu$ are shown in Figs. 5 and 6.

When the ST mode is $K^\mp\pi^\pm$, we form both the Cabibbo-favored (CF) combinations $\{K^-\pi^+, K^+\ell^-\bar{\nu}_\ell\}$ and $\{K^+\pi^-, K^-\ell^+\nu_\ell\}$ as well as the doubly Cabibbo-suppressed (DCS) combinations $\{K^-\pi^+, K^-\ell^+\nu_\ell\}$ and $\{K^+\pi^-, K^+\ell^-\bar{\nu}_\ell\}$. As shown in Section II, the ratio of CF and DCS yields gives a direct measurement of the squared amplitude ratio r^2 . For the DCS combinations, we place an additional requirement on the polar angle of the kaon in the $K^\mp\pi^\pm$ candidate of $|\cos\theta| < 0.8$. This requirement selects only kaons in the acceptance of the

TABLE VIII. DT yields and efficiencies including constituent branching fractions, for K_L^0 modes without $K_S^0\pi^+\pi^-$. Uncertainties are statistical only. All systematic uncertainties are correlated and are discussed in Section V.

Mode	Yield	Efficiency (%)
$K^-\pi^+, K_L^0\pi^0$	425 ± 21	29.9 ± 0.2
$K^+\pi^-, K_L^0\pi^0$	381 ± 20	31.1 ± 0.2
$K_S^0\pi^0, K_L^0\pi^0$	235 ± 15	14.6 ± 0.1
$K_S^0\eta, K_L^0\pi^0$	28.0 ± 5.4	5.34 ± 0.08
$K_S^0\omega, K_L^0\pi^0$	60.8 ± 8.7	5.33 ± 0.07
$K^-\pi^+, K_L^0\eta$	70.8 ± 8.6	11.2 ± 0.1
$K^+\pi^-, K_L^0\eta$	53.7 ± 7.6	11.5 ± 0.1
$K_S^0\pi^0, K_L^0\eta$	21.7 ± 4.8	5.55 ± 0.08
$K_S^0\eta, K_L^0\eta$	7.6 ± 2.8	2.01 ± 0.05
$K_S^0\omega, K_L^0\eta$	9.3 ± 3.5	2.04 ± 0.05
$K^-\pi^+, K_L^0\omega$	143 ± 13	12.1 ± 0.1
$K^+\pi^-, K_L^0\omega$	155 ± 14	12.2 ± 0.1
$K_S^0\pi^0, K_L^0\omega$	80.7 ± 9.8	5.70 ± 0.08
$K_S^0\eta, K_L^0\omega$	5.9 ± 3.2	2.06 ± 0.05
$K_S^0\omega, K_L^0\omega$	27.5 ± 5.6	1.86 ± 0.05
$K^-\pi^+, K_L^0\pi^0\pi^0$	157 ± 13	13.0 ± 0.1
$K^+\pi^-, K_L^0\pi^0\pi^0$	133 ± 12	13.2 ± 0.1
$K^+K^-, K_L^0\pi^0\pi^0$	57.1 ± 7.7	10.9 ± 0.1
$\pi^+\pi^-, K_L^0\pi^0\pi^0$	14.3 ± 4.9	14.5 ± 0.1
$K_S^0\pi^0\pi^0, K_L^0\pi^0\pi^0$	36.6 ± 6.5	2.85 ± 0.06

Ring Imaging Čerenkov counter (RICH), and it reduces the otherwise dominant background from misidentified Cabibbo-favored combinations to a negligible level. Figure 7 shows the summed U distributions for the two DCS $Ke\nu_e$ modes and the two DCS $K\mu\nu_\mu$ modes.

For $Ke\nu_e$ tagged with $K_S^0\pi^+\pi^-$, we consider sums of CF combinations $\{\bar{Y}_i, K^-\ell^+\nu_\ell\}$ and $\{Y_i, K^+\ell^-\bar{\nu}_\ell\}$, as well as sums of Cabibbo-suppressed (CS) combinations $\{Y_i, K^-\ell^+\nu_\ell\}$ and $\{\bar{Y}_i, K^+\ell^-\bar{\nu}_\ell\}$. We include the CF and CS $\{Y_i, Ke\nu_e\}$ yields measured in Ref. [29], and we perform a similar determination of CF and CS $\{Y_i, K\mu\nu_\mu\}$ yields where we select $K_S^0\pi^+\pi^-$ tags using the same criteria as in Ref. [29]. In analogy with $K^\mp\pi^\pm$ tags, the ratios of CF and CS yields probes the amplitude ratios ρ_i^2 , integrated over each phase space bin.

1. $Ke\nu_e$

For $Ke\nu_e$ modes, we require the fully reconstructed ST to have $1.8530 \text{ GeV}/c^2 < M < 1.8780 \text{ GeV}/c^2$ for $K_S^0\pi^0$ and $K_S^0\pi^0\pi^0$, $1.86 \text{ GeV}/c^2 < M < 1.87 \text{ GeV}/c^2$ for the DCS modes, and $1.8585 \text{ GeV}/c^2 < M < 1.8775 \text{ GeV}/c^2$ for all other modes. We identify electron candidates with the same criteria as in Ref. [12], via a multivariate discriminant that combines information from the ratio of the energy deposited in the calorimeter to the measured track momentum (E/p), ionization energy loss in the tracking chambers (dE/dx), and the

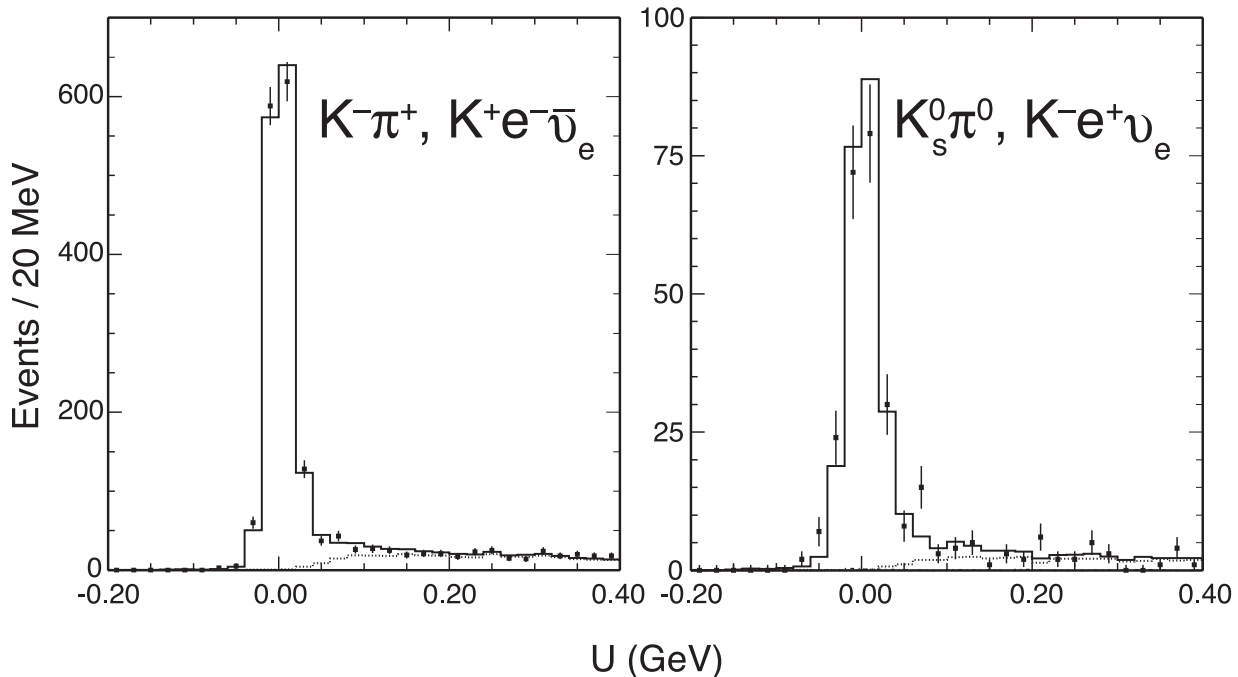


FIG. 5. Distributions of U for $\{K^-\pi^+, K^+e^-\bar{\nu}_e\}$ and $\{K_S^0\pi^0, K^-e^+\nu_e\}$. Data are shown as points with error bars. The solid lines show the total fits, and the dashed lines show the background components.

RICH. We fit the U distributions to signal and background probability distribution functions (PDFs) derived from simulated events and from sidebands in M and ΔE for the hadronic tag. For DCS modes, because of the low background, we simply count the number of events in the signal region $|U| < 0.352$ GeV, and we estimate a relative background contribution of $\mathcal{O}(10^{-3})$ from simulated events.

Table IX gives the semileptonic DT yields and efficiencies for modes without $K_S^0\pi^+\pi^-$. The uncorrelated systematic uncertainties are determined from yield excursions under variation of the signal and background shapes, histogram binning, and fit ranges. For DCS yields, we vary the size of the signal region by one-third, and we assign additional systematic uncertainties to the kaon polar-angle requirement and electron identification. Yields for $K e \nu_e$ tagged with $K_S^0\pi^+\pi^-$ (in 8 phase bins) are taken from Ref. [29].

2. $K\mu\nu_\mu$

For all $K\mu\nu_\mu$ modes, we require $1.86 \text{ GeV}/c^2 < M < 1.87 \text{ GeV}/c^2$ for the fully reconstructed ST. We select muon candidates using the same criteria as for charged pion candidates, except the particle identification requirements (on dE/dx and RICH) are applied to the muon mass hypothesis instead of the pion mass hypothesis. In reconstructing $K\mu\nu_\mu$, we reduce contamination from $K e \nu_e$ by requiring the muon momentum to be greater than $220 \text{ MeV}/c$, and we veto muon and kaon candidates that also satisfy the multivariate electron discriminant described in Section III D 1. Requiring $p_{\text{miss}} > 100 \text{ MeV}/c$ suppresses the $D \rightarrow K\pi$ background, for which p_{miss} peaks near zero. Finally, we reject events that

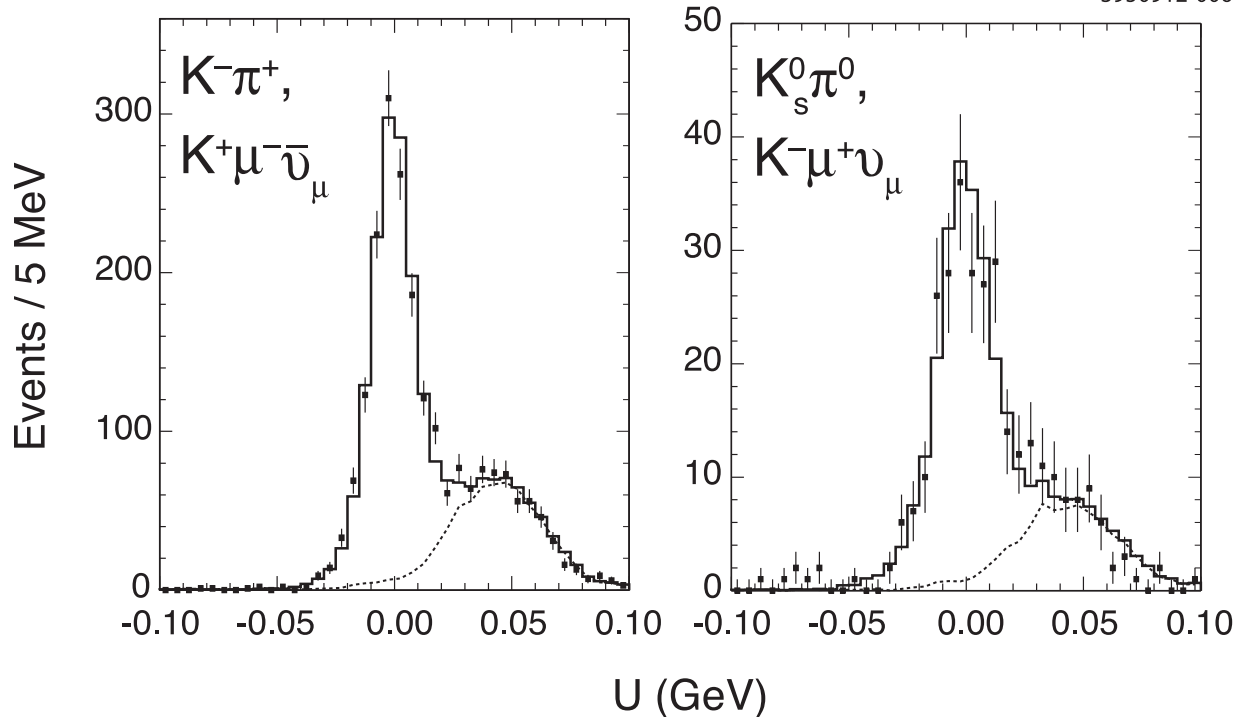


FIG. 6. Distributions of U for $\{K^-\pi^+, K^+\mu^-\bar{\nu}_\mu\}$ and $\{K_S^0\pi^0, K^-\mu^+\nu_\mu\}$. Data are shown as points with error bars. The solid lines show the total fits, and the dashed lines show the background components.

contain an additional shower with energy greater than 100 MeV, in order to reduce the $K^-\pi^+\pi^0$ background contribution. After this requirement, $K^-\pi^+\pi^0$ remains the dominant background, but it is kinematically separated in U from signal $K^-\mu^+\nu_\mu$ because of both the ν_μ - π^0 mass difference and the μ^+ - π^+ mass difference.

For all $K\mu\nu_\mu$ modes, including the DCS modes, we determine signal yields by fitting the U distributions to signal and background PDFs derived from simulated events. For the non-DCS modes, the background PDFs are smoothed to reduce the effect of statistical fluctuations in the simulated histograms. Tables X and XI give the semileptonic DT yields and efficiencies for modes with and without $K_S^0\pi^+\pi^-$, respectively. The uncorrelated systematic uncertainties are determined from yield excursions under variation of fit variations. For DCS yields, we also include systematic uncertainties for the kaon polar-angle requirement and the electron veto.

E. Events with $K e \nu_e$ and $K_L^0 \pi^0$

To reconstruct $\{K e \nu_e, K_L^0 \pi^0\}$, where both the ν_e and K_L^0 are undetected, we adopt the technique described in Refs. [37] and [38] for identifying events with two missing particles. Knowing the energy and momentum magnitude of the two D mesons in the initial state, and having reconstructed the K^\pm , e^\mp , and π^0 in the signal process, the direction of each D meson in the e^+e^- center of mass frame can be constrained to a cone around the flight direction of the $K^\pm e^\mp$ system or the π^0 . In signal events, the D^0 and \bar{D}^0 are collinear (within detector

TABLE IX. DT yields and efficiencies including constituent branching fractions, for $K e \nu_e$ modes without $K_S^0 \pi^+ \pi^-$. Yield uncertainties are statistical and uncorrelated systematic, respectively, and efficiency uncertainties are statistical only.

Mode	Yield	Efficiency (%)
$K^- \pi^+, K^+ e^- \bar{\nu}_e$	$1523 \pm 40 \pm 16$	37.9 ± 0.2
$K^+ \pi^-, K^+ e^- \bar{\nu}_e$	$5.0 \pm 2.2 \pm 0.9$	30.6 ± 0.2
$K^- K^+, K^+ e^- \bar{\nu}_e$	$156 \pm 13 \pm 4$	33.0 ± 0.5
$\pi^- \pi^+, K^+ e^- \bar{\nu}_e$	$70 \pm 9 \pm 5$	42.3 ± 0.9
$K_S^0 \pi^0 \pi^0, K^+ e^- \bar{\nu}_e$	$97 \pm 11 \pm 6$	10.6 ± 0.2
$K_S^0 \pi^0, K^+ e^- \bar{\nu}_e$	$245 \pm 16 \pm 15$	20.1 ± 0.3
$K_S^0 \eta, K^+ e^- \bar{\nu}_e$	$60 \pm 8 \pm 8$	6.7 ± 0.3
$K_S^0 \omega, K^+ e^- \bar{\nu}_e$	$76 \pm 11 \pm 9$	7.9 ± 0.2
$K^- \pi^+, K^- e^+ \nu_e$	$9.0 \pm 3.0 \pm 1.6$	29.8 ± 0.2
$K^+ \pi^-, K^- e^+ \nu_e$	$1603 \pm 42 \pm 23$	38.0 ± 0.2
$K^- K^+, K^- e^+ \nu_e$	$175 \pm 14 \pm 8$	33.6 ± 0.5
$\pi^- \pi^+, K^- e^+ \nu_e$	$64 \pm 8 \pm 1$	42.2 ± 0.9
$K_S^0 \pi^0 \pi^0, K^- e^+ \nu_e$	$108 \pm 12 \pm 6$	9.8 ± 0.2
$K_S^0 \pi^0, K^- e^+ \nu_e$	$244 \pm 16 \pm 5$	20.2 ± 0.3
$K_S^0 \eta, K^- e^+ \nu_e$	$35 \pm 6 \pm 2$	6.9 ± 0.3
$K_S^0 \omega, K^- e^+ \nu_e$	$73 \pm 10 \pm 8$	7.5 ± 0.2

TABLE X. DT yields and efficiencies including constituent branching fractions, for $K \mu \nu_\mu$ modes without $K_S^0 \pi^+ \pi^-$. Yield uncertainties are statistical and uncorrelated systematic, respectively, and efficiency uncertainties are statistical only.

Mode	Yield	Efficiency (%)
$K^- \pi^+, K^+ \mu^- \bar{\nu}_\mu$	$1442 \pm 40 \pm 13$	37.3 ± 0.2
$K^+ \pi^-, K^+ \mu^- \bar{\nu}_\mu$	$7.0 \pm 2.7 \pm 1.1$	34.8 ± 0.2
$K^- K^+, K^+ \mu^- \bar{\nu}_\mu$	$121 \pm 12 \pm 0$	32.9 ± 0.2
$\pi^- \pi^+, K^+ \mu^- \bar{\nu}_\mu$	$63.3 \pm 8.5 \pm 1.0$	42.7 ± 0.2
$K_S^0 \pi^0 \pi^0, K^+ \mu^- \bar{\nu}_\mu$	$85.2 \pm 10.6 \pm 4.7$	8.6 ± 0.1
$K_S^0 \pi^0, K^+ \mu^- \bar{\nu}_\mu$	$216 \pm 16 \pm 6$	18.3 ± 0.1
$K_S^0 \eta, K^+ \mu^- \bar{\nu}_\mu$	$37.7 \pm 6.4 \pm 0.2$	6.5 ± 0.1
$K_S^0 \omega, K^+ \mu^- \bar{\nu}_\mu$	$91.9 \pm 10.5 \pm 1.6$	7.1 ± 0.1
$K^- \pi^+, K^- \mu^+ \nu_\mu$	$9.8 \pm 3.5 \pm 1.6$	33.8 ± 0.2
$K^+ \pi^-, K^- \mu^+ \nu_\mu$	$1446 \pm 41 \pm 13$	38.0 ± 0.2
$K^- K^+, K^- \mu^+ \nu_\mu$	$175 \pm 14 \pm 0$	32.5 ± 0.2
$\pi^- \pi^+, K^- \mu^+ \nu_\mu$	$74.5 \pm 9.0 \pm 1.2$	41.7 ± 0.2
$K_S^0 \pi^0 \pi^0, K^- \mu^+ \nu_\mu$	$88.0 \pm 10.5 \pm 4.8$	8.5 ± 0.1
$K_S^0 \pi^0, K^- \mu^+ \nu_\mu$	$223 \pm 16 \pm 6$	18.1 ± 0.1
$K_S^0 \eta, K^- \mu^+ \nu_\mu$	$33.0 \pm 6.2 \pm 0.2$	6.5 ± 0.1
$K_S^0 \omega, K^- \mu^+ \nu_\mu$	$79.8 \pm 10.3 \pm 1.4$	7.2 ± 0.1

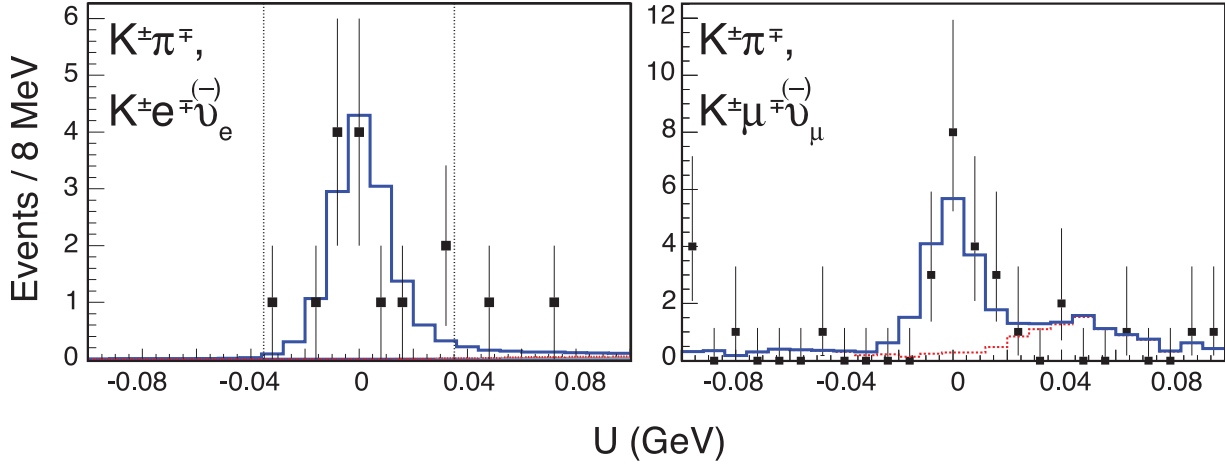


FIG. 7. Summed U distributions for $\{K^-\pi^+, K^-e^+\nu_e\}$ and $\{K^+\pi^-, K^+e^-\bar{\nu}_e\}$, as well as for $\{K^-\pi^+, K^-\mu^+\nu_\mu\}$ and $\{K^+\pi^-, K^+\mu^-\bar{\nu}_\mu\}$. Data are shown as points with error bars. For $Ke\nu_e$, the vertical lines mark the signal region, the solid histogram shows the simulated signal distribution normalized within the signal region to the number of observed events, and the small dashed histogram at large U values is the predicted background from simulation. For $K\mu\nu_\mu$, the solid histogram shows the total fit, and the dashed histogram shows the background component.

resolution), so when one of the cones is reflected through the origin, the two cones intersect. Background events typically have non-intersecting cones.

Following Ref. [38], we calculate the quantity

$$x_D^2 \equiv 1 - \frac{1}{\sin^2 \theta_{Ke,\pi^0}} \left(\cos^2 \theta_{D,Ke} + \cos^2 \theta_{D,\pi^0} + 2 \cos \theta_{Ke,\pi^0} \cos \theta_{D,Ke} \cos \theta_{D,\pi^0} \right), \quad (16)$$

where θ_{Ke,π^0} is the angle between the $K^\pm e^\mp$ system and the π^0 candidate, and $\theta_{D,Ke}$ and θ_{D,π^0} are the opening half-angles of the D cones around the $K^\pm e^\mp$ system and the π^0 , respectively. By construction, x_D^2 is less than or equal to 1, and when the cones do not intersect, then $x_D^2 < 0$. Signal events lie mostly in the range $0 \leq x_D^2 \leq 1$, with a small tail extending to $x_D^2 < 0$ due to mismeasurement.

In addition to the previously described criteria for K^\pm , e^\mp , and π^0 candidates, we recover electron bremsstrahlung photons by augmenting the electron four-momentum by any showers located within 100 mrad of the track direction and unassigned to any other particle. Also, kaons that satisfy the electron identification requirements are rejected.

We apply two additional requirements to suppress the background from radiative e^+e^- Bhabha scattering events: the electron momentum is required to be less than 1 GeV/ c , and the π^0 candidate must not have daughter showers that lie within 100 mrad of the electron candidate. To reduce the background from $\{Ke\nu_e, K_S^0\pi^0\}$ events, we reject events with extra tracks or π^0/η candidates.

Figure 8 shows the x_D^2 distribution, which is fitted to signal and background shapes from simulated events. The fitted yield is $764 \pm 36 \pm 23$, where the uncorrelated systematic uncertainty receives dominant contributions from the radiative Bhabha background determination, variations in background and signal shapes, and uncertainties in the modeling of extra tracks and π^0/η candidates. The signal efficiency determined from simulated events

TABLE XI. DT yields and efficiencies including constituent branching fractions, for $K\mu\nu_\mu$ modes with $K_S^0\pi^+\pi^-$. CF refers to the sum of Cabibbo-favored combinations $\{\bar{Y}_i, K^-\mu^+\nu_\mu\}$ and $\{Y_i, K^+\mu^-\bar{\nu}_\mu\}$. Similarly, CS refers to the sum of Cabibbo-suppressed combinations $\{Y_i, K^-\mu^+\nu_\mu\}$ and $\{\bar{Y}_i, K^+\mu^-\bar{\nu}_\mu\}$. Yield uncertainties are statistical and uncorrelated systematic, respectively, and efficiency uncertainties are statistical only.

Mode	Yield	Efficiency (%)
$Y_0, K\mu\nu_\mu$ (CF)	$162 \pm 14 \pm 2$	18.2 ± 0.2
$Y_1, K\mu\nu_\mu$ (CF)	$75.7 \pm 9.3 \pm 0.8$	18.4 ± 0.4
$Y_2, K\mu\nu_\mu$ (CF)	$132 \pm 13 \pm 1$	18.6 ± 0.3
$Y_3, K\mu\nu_\mu$ (CF)	$36.3 \pm 6.4 \pm 0.4$	18.9 ± 0.5
$Y_4, K\mu\nu_\mu$ (CF)	$67.7 \pm 8.8 \pm 0.7$	18.9 ± 0.3
$Y_5, K\mu\nu_\mu$ (CF)	$92.3 \pm 10.4 \pm 0.9$	17.8 ± 0.3
$Y_6, K\mu\nu_\mu$ (CF)	$120 \pm 12 \pm 1$	17.5 ± 0.3
$Y_7, K\mu\nu_\mu$ (CF)	$144 \pm 13 \pm 1$	17.8 ± 0.3
$Y_0, K\mu\nu_\mu$ (CS)	$66.0 \pm 8.5 \pm 0.7$	17.8 ± 0.4
$Y_1, K\mu\nu_\mu$ (CS)	$13.2 \pm 4.1 \pm 0.1$	17.9 ± 0.6
$Y_2, K\mu\nu_\mu$ (CS)	$33.0 \pm 6.2 \pm 0.3$	20.9 ± 0.8
$Y_3, K\mu\nu_\mu$ (CS)	$22.7 \pm 4.9 \pm 0.2$	20.0 ± 1.1
$Y_4, K\mu\nu_\mu$ (CS)	$46.8 \pm 7.3 \pm 0.5$	18.6 ± 0.6
$Y_5, K\mu\nu_\mu$ (CS)	$26.1 \pm 5.7 \pm 0.3$	18.8 ± 0.7
$Y_6, K\mu\nu_\mu$ (CS)	$21.1 \pm 5.0 \pm 0.2$	17.0 ± 0.7
$Y_7, K\mu\nu_\mu$ (CS)	$58.1 \pm 8.2 \pm 0.6$	17.7 ± 0.4

is $(34.58 \pm 0.04)\%$.

F. Crossfeed and Peaking Backgrounds

As in Ref. [12], crossfeed among signal modes and peaking background contributions are subtracted by the fitter, using crossfeed probabilities and background efficiencies determined from simulated events, as well as branching fractions for peaking background processes [39]. These inputs are listed in Tables XII and XIII, and we account for correlated uncertainties among them. Backgrounds in DT modes are assumed to contribute at the same rate as for ST modes, with corrections for quantum correlation effects. When a ST background process does not exactly match the particle content of the corresponding signal process, then that background does not contribute to DT modes because of the additional constraints imposed by DT reconstruction. In general, peaking backgrounds contribute less than 1% to the measured yields, except in $K_L^0\pi^0$ modes (1–2%), $K_L^0\eta$ modes (2–5%), $\{K\ell\nu_\ell, K_L^0\pi^0\}$ (1%), ST $K_S^0\pi^0\pi^0$ (3%), Cabibbo-favored $\{K_S^0\pi^+\pi^-, K_S^0\pi^+\pi^-\}$ (1–19%), and Cabibbo-suppressed $\{K_S^0\pi^+\pi^-, K_S^0\pi^+\pi^-\}$ (2–56%). The large background fractions in the last two categories occur in modes with small numbers of observed events.

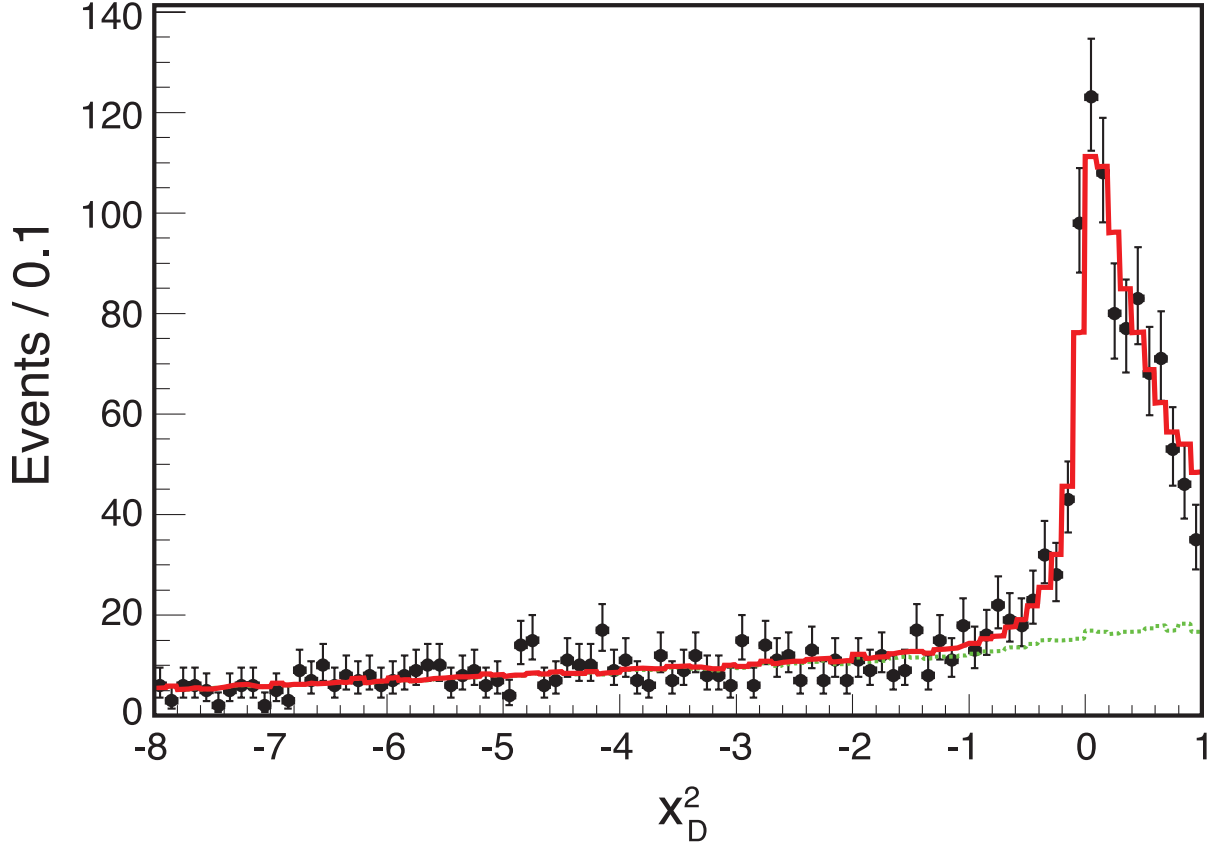


FIG. 8. Distribution of x_D^2 for $\{K\ell\nu_e, K_L^0\pi^0\}$. Data are shown as points with error bars. The solid line shows the total fit, and the dashed line shows the sum of background components.

IV. EXTERNAL MEASUREMENTS

Unlike our previous analysis in Ref. [12], we do not include any external branching fraction or R_{WS} measurements in the fit. With our increased data sample, branching fraction measurements from other experiments do not have a significant impact on our precision, and our direct measurement of r^2 (from DCS $\{K\pi, K\ell\nu_\ell\}$) obviates the need for input on r^2 from R_{WS} . We do, however, include the external measurements of mixing parameters shown in Table XIV, where $x'^2 \equiv 2R_M - y'^2$. Averages from Ref. [27] in this Table do not include previous CLEO-c results. Correlation coefficients that are not shown in Table XIV are taken to be zero. Also, since we neglect CP violation, we assume $y_{CP} = y$. In the fit, we use the signed measurement of x along with y' to resolve the sign ambiguity in $\sin\delta$ and the s_i , even though we quote a fitted value only for x^2 .

V. SYSTEMATIC UNCERTAINTIES

We include systematic uncertainties directly in the fit. Uncorrelated uncertainties for each yield are discussed above in Section III. Correlated uncertainties are given in Tables XV and XVI. When the fit is performed without external measurements, these correlated uncer-

TABLE XII. Crossfeed probabilities among signal modes. Ranges are given for groups of modes.

Crossfeed \rightarrow Signal	Efficiency (%)
$K^+\pi^- \rightarrow K^-\pi^+$	0.088 ± 0.002
$K^-\pi^+ \rightarrow K^+\pi^-$	0.089 ± 0.002
$K_S^0\omega \rightarrow K_S^0\pi^0\pi^0$	0.080 ± 0.003
$K^-\pi^+, K_S^0\pi^0 \rightarrow K^-\pi^+, K_L^0\pi^0$	0.45 ± 0.02
$K^+\pi^-, K_S^0\pi^0 \rightarrow K^+\pi^-, K_L^0\pi^0$	0.43 ± 0.02
$K^-\pi^+, K_S^0\eta \rightarrow K^-\pi^+, K_L^0\eta$	0.13 ± 0.01
$K^+\pi^-, K_S^0\eta \rightarrow K^+\pi^-, K_L^0\eta$	0.12 ± 0.01
$K^-\pi^+, K_L^0\pi^0 \rightarrow K^-\pi^+, K_L^0\eta$	0.14 ± 0.01
$K^+\pi^-, K_L^0\pi^0 \rightarrow K^+\pi^-, K_L^0\eta$	0.13 ± 0.01
$K_S^0\pi^0, K_L^0\pi^0 \rightarrow K_S^0\pi^0, K_L^0\eta$	0.06 ± 0.01
$K_S^0\eta, K_L^0\pi^0 \rightarrow K_S^0\eta, K_L^0\eta$	0.04 ± 0.01
$K_S^0\omega, K_L^0\pi^0 \rightarrow K_S^0\omega, K_L^0\eta$	0.03 ± 0.01
$K^-\pi^+, K_S^0\omega \rightarrow K^-\pi^+, K_L^0\omega$	0.13 ± 0.01
$K^+\pi^-, K_S^0\omega \rightarrow K^+\pi^-, K_L^0\omega$	0.12 ± 0.01
$K^-\pi^+, K_S^0\pi^0\pi^0 \rightarrow K^-\pi^+, K_L^0\pi^0\pi^0$	0.47 ± 0.02
$K^+\pi^-, K_S^0\pi^0\pi^0 \rightarrow K^+\pi^-, K_L^0\pi^0\pi^0$	0.46 ± 0.02
$K^-\pi^+, K_S^0\pi^0 \rightarrow K^-\pi^+, K_L^0\pi^0\pi^0$	0.61 ± 0.03
$K^+\pi^-, K_S^0\pi^0 \rightarrow K^+\pi^-, K_L^0\pi^0\pi^0$	0.62 ± 0.03
$K^+K^-, K_S^0\pi^0 \rightarrow K^+K^-, K_L^0\pi^0\pi^0$	0.49 ± 0.02
$\pi^+\pi^-, K_S^0\pi^0 \rightarrow \pi^+\pi^-, K_L^0\pi^0\pi^0$	0.68 ± 0.03
$K_S^0\pi^0\pi^0, K_S^0\pi^0 \rightarrow K_S^0\pi^0\pi^0, K_L^0\pi^0\pi^0$	0.16 ± 0.01
$K^-\pi^+, K_L^0\pi^0 \rightarrow K^-\pi^+, K_L^0\pi^0\pi^0$	0.11 ± 0.01
$K^+\pi^-, K_L^0\pi^0 \rightarrow K^+\pi^-, K_L^0\pi^0\pi^0$	0.12 ± 0.01
$Ke\nu_e, K_S^0\pi^0 \rightarrow Ke\nu_e, K_L^0\pi^0$	2.31 ± 0.03
$K^-\pi^+, K^+e^-\bar{\nu}_e \rightarrow K^-\pi^+, K^-e^+\nu_e$	0.0048 ± 0.0022
$K^+\pi^-, K^-e^+\nu_e \rightarrow K^-\pi^+, K^-e^+\nu_e$	0.0057 ± 0.0025
$K^-\pi^+, K^+e^-\bar{\nu}_e \rightarrow K^+\pi^-, K^+e^-\bar{\nu}_e$	0.0038 ± 0.0020
$K^+\pi^-, K^-e^+\nu_e \rightarrow K^+\pi^-, K^+e^-\bar{\nu}_e$	0.0019 ± 0.0014
$K^-\pi^+, K^+\mu^-\bar{\nu}_\mu \rightarrow K^-\pi^+, K^-\mu^+\nu_\mu$	0.0029 ± 0.0017
$K^+\pi^-, K^-\mu^+\nu_\mu \rightarrow K^-\pi^+, K^-\mu^+\nu_\mu$	0.0067 ± 0.0026
$K^-\pi^+, K^+\mu^-\bar{\nu}_\mu \rightarrow K^+\pi^-, K^+\mu^-\bar{\nu}_\mu$	0.0019 ± 0.0014
$K^+\pi^-, K^-\mu^+\nu_\mu \rightarrow K^+\pi^-, K^+\mu^-\bar{\nu}_\mu$	0.0010 ± 0.0010
$K_S^0\eta, K\mu\nu_\mu \rightarrow K_S^0\pi^+\pi^-, K\mu\nu_\mu$	$(0-3) \times 10^{-3}$
$K_S^0\omega, K\mu\nu_\mu \rightarrow K_S^0\pi^+\pi^-, K\mu\nu_\mu$	$(0-5) \times 10^{-2}$

tainties cancel in all the fit parameters except \mathcal{N} and the branching fractions. Uncertainties on the peaking background branching fractions in Table XIII and the external measurements in Table XIV are also included as systematic uncertainties.

In Table XV, we list the correlated systematic uncertainties on reconstruction and particle identification efficiencies for individual final state particles. Those for π^\pm , K^\pm , π^0 , K_S^0 , and e^\pm reconstruction and particle identification (PID) are determined using the techniques described in Refs. [41, 42]. For K_S^0 , we include additional contributions for the flight signifi-

TABLE XIII. Peaking background branching fractions and efficiencies including constituent branching fractions. Ranges are given for groups of modes. Fully reconstructed hadronic tag modes are denoted by X . Backgrounds marked by an asterisk (*) occur only in STs, not DTs.

Background \rightarrow Signal	\mathcal{B}_{bkg} (%) [39]	Efficiency (%)
$K_S^0\pi^+\pi^- \rightarrow K_S^0\pi^0\pi^0$	2.94 ± 0.16	0.0076 ± 0.005
$K^-\pi^+\pi^0$ (*) $\rightarrow K_S^0\pi^0\pi^0$	13.9 ± 0.5	0.0027 ± 0.0001
$D^+ \rightarrow K_S^0\pi^+\pi^0$ (*) $\rightarrow K_S^0\pi^0\pi^0$	6.90 ± 0.32	0.0594 ± 0.0010
$\rho^+\pi^- \rightarrow K_S^0\pi^0$	1.447 ± 0.046	0.078 ± 0.004
$\rho^0\pi^0 \rightarrow K_S^0\pi^0$	0.373 ± 0.022	0.011 ± 0.004
Generic $D^0\bar{D}^0$ (*) $\rightarrow K_S^0\pi^0$	100	0.0006 ± 0.0001
Generic D^+D^- (*) $\rightarrow K_S^0\pi^0$	100	0.0003 ± 0.0002
$\eta\pi^0, X \rightarrow K_L^0\pi^0, X$	0.064 ± 0.011	0.3–1.4
$\pi^0\pi^0, X \rightarrow K_L^0\pi^0, X$	0.080 ± 0.008	0.8–4.3
$\eta\pi^0, X \rightarrow K_L^0\eta, X$	0.064 ± 0.011	0.1–0.3
$\eta\eta, X \rightarrow K_L^0\eta, X$	0.167 ± 0.019	0.2–0.8
$Ke\nu_e, K_L^0\pi^0\pi^0 \rightarrow Ke\nu_e, K_L^0\pi^0$	From fitter	0.45 ± 0.04
$K_L^0\pi^+\pi^-, K\mu\nu_\mu \rightarrow K_S^0\pi^+\pi^-, K\mu\nu_\mu$	2.94 ± 0.16	$(0-6) \times 10^{-3}$
$\pi^+\pi^-\pi^+\pi^-, X \rightarrow K_S^0\pi^+\pi^-, X$	0.744 ± 0.021	$(1-25) \times 10^{-2}$

TABLE XIV. External measurements of y_{CP} , x , y , r^2 , y' and x'^2 . Correlation coefficients ρ are for the measurements in the same column.

Parameter	Value(s) (%)		
y_{CP}	1.064 ± 0.209 [27]		
x	0.419 ± 0.211 [27]		
y	0.456 ± 0.186 [27]		
r^2	0.364 ± 0.017 [8]	$0.303 \pm 0.016 \pm 0.010$ [9]	0.304 ± 0.055 [10]
y'	$0.06^{+0.40}_{-0.39}$ [8]	$0.97 \pm 0.44 \pm 0.31$ [9]	0.85 ± 0.76 [10]
x'^2	$0.018^{+0.021}_{-0.023}$ [8]	$-0.022 \pm 0.030 \pm 0.021$ [9]	-0.012 ± 0.035 [10]
$\rho(r^2, y')$	-83.4 [40]	-87 [40]	-97.1 [40]
$\rho(r^2, x'^2)$	$+65.5$ [40]	$+77$ [40]	$+92.3$ [40]
$\rho(y', x'^2)$	-90.9 [40]	-94 [40]	-98.4 [40]

cance and invariant mass requirements. For η , we use the same uncertainties as in Ref. [12]. The K_L^0 uncertainties are determined by varying the selection requirements. The above studies also provide efficiency corrections, which are included in the signal and background efficiencies listed in this paper.

Table XVI shows mode-dependent uncertainties, including those for initial state radiation (ISR), final state radiation (FSR), and selection requirements in two-track modes that veto radiative Bhabhas and cosmic muons. Most of the uncertainties in Table XVI are determined with the same techniques as in Ref. [12], updated to the current data and simulated samples. We assess uncertainties for new modes by relaxing selection requirements and noting the resultant change in efficiency-corrected yield.

TABLE XV. Correlated, fractional efficiency systematic uncertainties and the schemes for applying them in the fit.

Source	Uncertainty (%)	Scheme
Track finding	0.3	per track
K^\pm hadronic interactions	0.5	per K^\pm
K_S^0 finding	0.9	per K_S^0
π^0 finding	2.0	per π^0
η finding	4.0	per η
dE/dx and RICH	0.1	per π^\pm PID cut
dE/dx and RICH	0.1	per K^\pm PID cut
Electron identification	0.4	per e^\pm
K_L^0 shower veto	0.4	per K_L^0
K_L^0 background subtraction	0.7	per K_L^0
K_L^0 track veto	0.3	per K_L^0
K_L^0 signal shape	1.4	per K_L^0

TABLE XVI. Correlated, mode-dependent fractional systematic uncertainties in percent for STs. An asterisk (*) marks those uncertainties that are correlated among modes. The schemes by which these uncertainties are applied to DTs are also given, along with the fractional DT uncertainty, λ_{DT} , on mode $\{A, B\}$ for ST uncertainties of α on mode A and β on mode B .

	ΔE	ISR*	FSR*	Lepton Veto*	Other
$K^\mp \pi^\pm$	0.5	0.5	0.9	0.5	
$K^+ K^-$	0.9	0.5	0.5	0.4	0.5 $K^\pm \cos \theta$ cut
$\pi^+ \pi^-$	1.9	0.5	1.4	3.2	
$K_S^0 \pi^0 \pi^0$	2.6	0.5			1.5 K_S^0 daughter PID 0.7 resonant substructure
$K_S^0 \pi^0$	0.9	0.5			
$K_S^0 \eta$	5.5	0.5			0.3 η mass cut 0.7 $\mathcal{B}(\eta \rightarrow \gamma\gamma)$ [39]
$K_S^0 \omega$	1.2	0.5	0.6		0.1 ω mass cut/SB subt. 0.8 $\mathcal{B}(\omega \rightarrow \pi^+ \pi^- \pi^0)$ [39]
$K_L^0 \pi^0 (\pi^0)$		0.5			
$K_L^0 \eta$		0.5			1.6 extra π^0 veto
$K_L^0 \omega$		0.5	0.6		0.1 ω mass cut/SB subt. 0.8 $\mathcal{B}(\omega \rightarrow \pi^+ \pi^- \pi^0)$ [39]
$K_S^0 \pi^+ \pi^-$	0.9	0.5	1.4		
$K \nu_e$		0.5	0.3		2.0 spectrum extrapolation
$K \mu \nu_\mu$		0.5	0.3		2.0 spectrum extrapolation 0.4 extra shower veto
Scheme	per D	per yield	per D	per ST	per D
λ_{DT}	$\sqrt{\alpha^2 + \beta^2}$	$(\alpha + \beta)/2$	$\alpha + \beta$	0	$\sqrt{\alpha^2 + \beta^2}$

VI. FIT RESULTS

We combine the 261 yield measurements discussed above, along with estimates of efficiencies and background contributions, in a χ^2 fit that determines 51 free parameters: \mathcal{N} ; y ; r^2 ; $\cos \delta$; $\sin \delta$; x^2 ; ρ_i^2 , c_i , and s_i for each of the 8 phase bins in $K_S^0 \pi^+ \pi^-$; and 21 branching fractions. We tested the analysis technique using a simulated sample of quantum-correlated $D^0 \bar{D}^0$ decays with an effective integrated luminosity of 10 times our data sample. In Tables XVII and XVIII, we show the results of two fits: one with no external inputs (Standard Fit) and one including the measurements in Table XIV (Extended Fit). The fits are performed using both statistical and systematic uncertainties on the input measurements. We evaluate statistical uncertainties on the fit parameters by performing a second set of fits using only statistical uncertainties on the inputs. Then, we compute the systematic uncertainty on a given fit parameter by taking the quadrature difference between its total uncertainty and its statistical uncertainty. When a fit parameter is directly constrained by an external measurement, we quote only one uncertainty. Asymmetric uncertainties are determined from the likelihood scans discussed below. Table XIX gives the correlation coefficients for y , r^2 , $\cos \delta$, $\sin \delta$, and x^2 . The full correlation matrices can be found on EPAPS [43].

These results include the first direct measurement of $\sin \delta$, as well as first branching fraction measurements for $D^0 \rightarrow K_L^0 \eta$, $K_L^0 \omega$, and $K_L^0 \pi^0 \pi^0$. We also present the first CLEO-c branching fraction measurement for $D^0 \rightarrow K^- \mu^+ \nu_\mu$. In the Standard Fit, the statistical uncertainties on y and $r \cos \delta$ are approximately three times smaller than in our previous analysis [12]. Because of the strong correlation between r^2 and $\cos \delta$, and because r^2 is determined by different inputs in the two analyses, a direct comparison of the $\cos \delta$ uncertainties is not instructive. Accounting for correlated uncertainties, the results for $\cos \delta$ in the Standard and Extended Fits differ by 2.5σ . This difference is caused primarily by the upward fluctuations in y and r^2 in the Standard Fit, which are both negatively correlated with $\cos \delta$. Also, the Extended Fit demonstrates that when our $\cos \delta$ and $\sin \delta$ measurements are used to combine y and y' from other experiments, the overall uncertainty on y is reduced by approximately 10% compared to the global average of all measurements in Table XIV (except y_{CP} from Ref. [5]) found in Ref. [40]: $y = 0.79 \pm 0.13$. Note that this global average includes the results from Ref. [12].

Figure 9 shows the one-dimensional posterior PDFs for $\cos \delta$, $\sin \delta$, δ , and y in the Standard Fit, including statistical and systematic uncertainties. These curves are obtained by re-minimizing the χ^2 at each point and computing $\mathcal{L} = e^{-(\chi^2 - \chi_{\min}^2)/2}$. Also shown are the two-dimensional contours for combinations of y , $\cos \delta$, and $\sin \delta$. Because of the $\sin \delta$ sign ambiguity, the PDFs for both $\sin \delta$ and δ in the Standard Fit are symmetric around zero. Figure 10 shows the same distributions for the Extended Fit. Here, the sign ambiguity is resolved by the external measurements. All the PDFs, except those for δ , are well described by Gaussians or bifurcated Gaussians. In particular, the non-Gaussian profile for $\cos \delta$ in the Standard Fit from Ref. [12] has been eliminated by our direct measurement of r^2 .

Although the central value for $\cos \delta$ in the Extended Fit is unphysical, we find $\tau \equiv (\cos^2 \delta + \sin^2 \delta)^{1/2} = 1.28 \pm 0.27$ to be consistent with physical boundary. Similarly, in the Standard Fit, $\tau = 0.81 \pm 0.21$. The PDFs for δ in Figs. 9 and 10 are obtained by probing $\cos \delta$ and $\sin \delta$ under the constraint $\tau = 1$, which reduces the height of the PDF relative to the other parameters. The implied values for δ from these PDFs are $|\delta| = (10_{-53}^{+28+13})^\circ$ for the Standard Fit and $\delta = (18_{-17}^{+11})^\circ$ for the Extended Fit. Also, applying the above constraint in the Standard Fit improves the uncertainties on y and x^2 by 15% and 8%, respectively,

TABLE XVII. Results from the Standard Fit and the Extended Fit for all parameters except branching fractions. Uncertainties are statistical and systematic, respectively. In the Extended Fit, we quote only one uncertainty for y , r^2 , and x^2 , which are directly constrained by an external measurement.

Parameter	Standard Fit	Extended Fit
\mathcal{N} (10^6)	$3.092 \pm 0.050 \pm 0.040$	$3.114 \pm 0.050 \pm 0.040$
y (%)	$4.2 \pm 2.0 \pm 1.0$	0.636 ± 0.114
r^2 (%)	$0.533 \pm 0.107 \pm 0.045$	0.333 ± 0.008
$\cos \delta$	$0.81^{+0.22+0.07}_{-0.18-0.05}$	$1.15^{+0.19+0.00}_{-0.17-0.08}$
$\sin \delta$	$-0.01 \pm 0.41 \pm 0.04$	$0.56^{+0.32+0.21}_{-0.31-0.20}$
x^2 (%)	$0.06 \pm 0.23 \pm 0.11$	0.0022 ± 0.0023
ρ_0^2	$0.337 \pm 0.030 \pm 0.006$	$0.352 \pm 0.032 \pm 0.005$
ρ_1^2	$0.270 \pm 0.044 \pm 0.005$	$0.280 \pm 0.047 \pm 0.000$
ρ_2^2	$0.235 \pm 0.028 \pm 0.003$	$0.252 \pm 0.028 \pm 0.004$
ρ_3^2	$0.399 \pm 0.066 \pm 0.005$	$0.416 \pm 0.069 \pm 0.000$
ρ_4^2	$0.592 \pm 0.067 \pm 0.010$	$0.623 \pm 0.071 \pm 0.000$
ρ_5^2	$0.343 \pm 0.044 \pm 0.000$	$0.329 \pm 0.040 \pm 0.008$
ρ_6^2	$0.146 \pm 0.023 \pm 0.000$	$0.145 \pm 0.023 \pm 0.000$
ρ_7^2	$0.445 \pm 0.039 \pm 0.002$	$0.439 \pm 0.039 \pm 0.003$
c_0	$-0.76 \pm 0.06 \pm 0.01$	$-0.73 \pm 0.06 \pm 0.01$
c_1	$-0.75 \pm 0.11 \pm 0.00$	$-0.72 \pm 0.11 \pm 0.02$
c_2	$0.00 \pm 0.10 \pm 0.01$	$0.03 \pm 0.10 \pm 0.02$
c_3	$0.45 \pm 0.15 \pm 0.01$	$0.47 \pm 0.14 \pm 0.01$
c_4	$0.95 \pm 0.07 \pm 0.01$	$0.95 \pm 0.07 \pm 0.00$
c_5	$0.79 \pm 0.09 \pm 0.01$	$0.81 \pm 0.09 \pm 0.00$
c_6	$-0.20 \pm 0.13 \pm 0.02$	$-0.16 \pm 0.13 \pm 0.01$
c_7	$-0.41 \pm 0.07 \pm 0.01$	$-0.39 \pm 0.07 \pm 0.01$
s_0	$0.55 \pm 0.16 \pm 0.00$	$0.61 \pm 0.15 \pm 0.02$
s_1	$0.53 \pm 0.28 \pm 0.00$	$0.56 \pm 0.27 \pm 0.03$
s_2	$0.93 \pm 0.15 \pm 0.00$	$0.91 \pm 0.15 \pm 0.02$
s_3	$0.47 \pm 0.30 \pm 0.00$	$0.52 \pm 0.29 \pm 0.01$
s_4	$0.55 \pm 0.24 \pm 0.00$	$0.60 \pm 0.23 \pm 0.02$
s_5	$-0.71 \pm 0.24 \pm 0.00$	$-0.69 \pm 0.24 \pm 0.00$
s_6	$-0.42 \pm 0.27 \pm 0.06$	$-0.17 \pm 0.29 \pm 0.03$
s_7	$-0.30 \pm 0.18 \pm 0.04$	$-0.21 \pm 0.19 \pm 0.03$
$\chi_{\text{fit}}^2/\text{ndof}$	193.2/210	214.7/222

resulting in $y = (3.3 \pm 1.7 \pm 0.8)\%$ and $x^2 = (0.14 \pm 0.21 \pm 0.09)\%$; the changes in all other parameters are negligible. Performing the Extended Fit with $\tau = 1$ produces negligible shifts in all the fit parameters.

Our results for c_i , s_i , and branching fractions do not supersede other CLEO-c measurements. For c_i and s_i , our fitted values are consistent with those in Ref. [29], after accounting for differences between the two analyses.

TABLE XVIII. Branching fraction results from the Standard Fit and the Extended Fit. Uncertainties are statistical and systematic, respectively.

Parameter	Standard Fit	Extended Fit
$\mathcal{B}(K^- \pi^+)$ (%)	$3.77 \pm 0.06 \pm 0.05$	$3.76 \pm 0.06 \pm 0.05$
$\mathcal{B}(K^- K^+)$ (10^{-3})	$3.99 \pm 0.07 \pm 0.08$	$3.98 \pm 0.07 \pm 0.08$
$\mathcal{B}(\pi^- \pi^+)$ (10^{-3})	$1.36 \pm 0.03 \pm 0.04$	$1.37 \pm 0.03 \pm 0.04$
$\mathcal{B}(K_S^0 \pi^0 \pi^0)$ (%)	$0.99 \pm 0.02 \pm 0.06$	$0.99 \pm 0.02 \pm 0.06$
$\mathcal{B}(K_L^0 \pi^0)$ (%)	$0.94 \pm 0.03 \pm 0.03$	$0.96 \pm 0.03 \pm 0.03$
$\mathcal{B}(K_L^0 \eta)$ (10^{-3})	$3.36 \pm 0.30 \pm 0.17$	$3.40 \pm 0.31 \pm 0.17$
$\mathcal{B}(K_L^0 \omega)$ (%)	$0.90 \pm 0.05 \pm 0.03$	$0.91 \pm 0.05 \pm 0.03$
$\mathcal{B}(K_S^0 \pi^0)$ (%)	$1.17 \pm 0.02 \pm 0.03$	$1.16 \pm 0.02 \pm 0.03$
$\mathcal{B}(K_S^0 \eta)$ (10^{-3})	$4.95 \pm 0.14 \pm 0.36$	$4.90 \pm 0.14 \pm 0.36$
$\mathcal{B}(K_S^0 \omega)$ (%)	$1.15 \pm 0.02 \pm 0.04$	$1.14 \pm 0.02 \pm 0.04$
$\mathcal{B}(K_L^0 \pi^0 \pi^0)$ (%)	$0.95 \pm 0.06 \pm 0.05$	$0.94 \pm 0.06 \pm 0.05$
$\mathcal{B}(K^- e^+ \nu_e)$ (%)	$3.54 \pm 0.05 \pm 0.08$	$3.52 \pm 0.05 \pm 0.08$
$\mathcal{B}(K^- \mu^+ \nu_\mu)$ (%)	$3.38 \pm 0.05 \pm 0.08$	$3.36 \pm 0.05 \pm 0.08$
$\mathcal{B}(Y_0)$ (10^{-3})	$4.38 \pm 0.18 \pm 0.12$	$4.33 \pm 0.17 \pm 0.11$
$\mathcal{B}(Y_1)$ (10^{-3})	$1.65 \pm 0.10 \pm 0.04$	$1.63 \pm 0.10 \pm 0.04$
$\mathcal{B}(Y_2)$ (10^{-3})	$3.43 \pm 0.16 \pm 0.10$	$3.33 \pm 0.14 \pm 0.08$
$\mathcal{B}(Y_3)$ (10^{-3})	$0.99 \pm 0.08 \pm 0.03$	$0.97 \pm 0.08 \pm 0.02$
$\mathcal{B}(Y_4)$ (10^{-3})	$1.70 \pm 0.11 \pm 0.05$	$1.62 \pm 0.10 \pm 0.04$
$\mathcal{B}(Y_5)$ (10^{-3})	$2.11 \pm 0.13 \pm 0.07$	$2.13 \pm 0.12 \pm 0.05$
$\mathcal{B}(Y_6)$ (10^{-3})	$3.15 \pm 0.15 \pm 0.08$	$3.14 \pm 0.14 \pm 0.08$
$\mathcal{B}(Y_7)$ (10^{-3})	$3.68 \pm 0.16 \pm 0.09$	$3.71 \pm 0.16 \pm 0.09$

VII. SUMMARY

We present an updated analysis of quantum correlations in $D^0 \bar{D}^0$ decays at the $\psi(3770)$ using the full CLEO-c dataset, resulting in a new value of $\cos \delta = 0.81_{-0.18-0.05}^{+0.22+0.07}$ and a first measurement of $\sin \delta = -0.01 \pm 0.41 \pm 0.04$, which, when combined, imply a strong phase of $|\delta| = (10_{-53-0}^{+28+13})^\circ$. By including external inputs on mixing parameters in the fit, we find alternative values of $\cos \delta = 1.15_{-0.17-0.08}^{+0.19+0.00}$, $\sin \delta = 0.56_{-0.31-0.20}^{+0.32+0.21}$, and $\delta = (18_{-17}^{+11})^\circ$. The effect of these measurements on the world averages of mixing parameters is to improve the uncertainty on y by approximately 10%.

ACKNOWLEDGMENTS

We gratefully acknowledge the effort of the CESR staff in providing us with excellent luminosity and running conditions. This work was supported by the National Science Foundation, the U.S. Department of Energy, the Natural Sciences and Engineering Research

TABLE XIX. Correlation coefficients (%) for the fits in Table XVII using both statistical and systematic uncertainties.

	y	r^2	$\cos \delta$	$\sin \delta$
Standard Fit				
r^2		0		
$\cos \delta$	-53	-42		
$\sin \delta$	-3	+1	+4	
x^2	-73	0	+39	+2
Extended Fit				
r^2		+3		
$\cos \delta$	-27	-16		
$\sin \delta$	+62	+21	+36	
x^2	+9	+25	+5	-18

Council of Canada, and the U.K. Science and Technology Facilities Council.

-
- [1] M. Staric *et al.* [Belle Collaboration], Phys. Rev. Lett. **98**, 211803 (2007) [arXiv:hep-ex/0703036].
 - [2] B. Aubert *et al.* [BABAR Collaboration], Phys. Rev. D **78**, 011105 (2008) [arXiv:0712.2249 [hep-ex]].
 - [3] B. Aubert *et al.* [BABAR Collaboration], Phys. Rev. D **80**, 071103 (2009) [arXiv:0908.0761 [hep-ex]].
 - [4] A. Zupanc *et al.* [Belle Collaboration], Phys. Rev. D **80**, 052006 (2009) [arXiv:0905.4185 [hep-ex]].
 - [5] R. Aaij *et al.* [LHCb Collaboration], JHEP **1204**, 129 (2012) [arXiv:1112.4698 [hep-ex]].
 - [6] L. M. Zhang *et al.* [BELLE Collaboration], Phys. Rev. Lett. **99**, 131803 (2007) [arXiv:0704.1000 [hep-ex]].
 - [7] P. del Amo Sanchez *et al.* [BABAR Collaboration], Phys. Rev. Lett. **105**, 081803 (2010) [arXiv:1004.5053 [hep-ex]].
 - [8] L. M. Zhang *et al.* [Belle Collaboration], Phys. Rev. Lett. **96**, 151801 (2006) [arXiv:hep-ex/0601029].
 - [9] B. Aubert *et al.* [BABAR Collaboration], Phys. Rev. Lett. **98**, 211802 (2007) [arXiv:hep-ex/0703020].
 - [10] T. Aaltonen *et al.* [CDF Collaboration], Phys. Rev. Lett. **100**, 121802 (2008) [arXiv:0712.1567 [hep-ex]].
 - [11] M. Gronau, Y. Grossman and J. L. Rosner, Phys. Lett. B **508**, 37 (2001) [arXiv:hep-ph/0103110].
 - [12] J. L. Rosner *et al.* [CLEO Collaboration], Phys. Rev. Lett. **100**, 221801 (2008) [arXiv:0802.2264 [hep-ex]]; D. M. Asner *et al.* [CLEO Collaboration], Phys. Rev. D **78**, 012001 (2008) [arXiv:0802.2268 [hep-ex]].
 - [13] R. L. Kingsley, S. B. Treiman, F. Wilczek and A. Zee, Phys. Rev. D **11**, 1919 (1975).
 - [14] L. B. Okun, B. M. Pontecorvo and V. I. Zakharov, Lett. Nuovo Cim. **13**, 218 (1975).

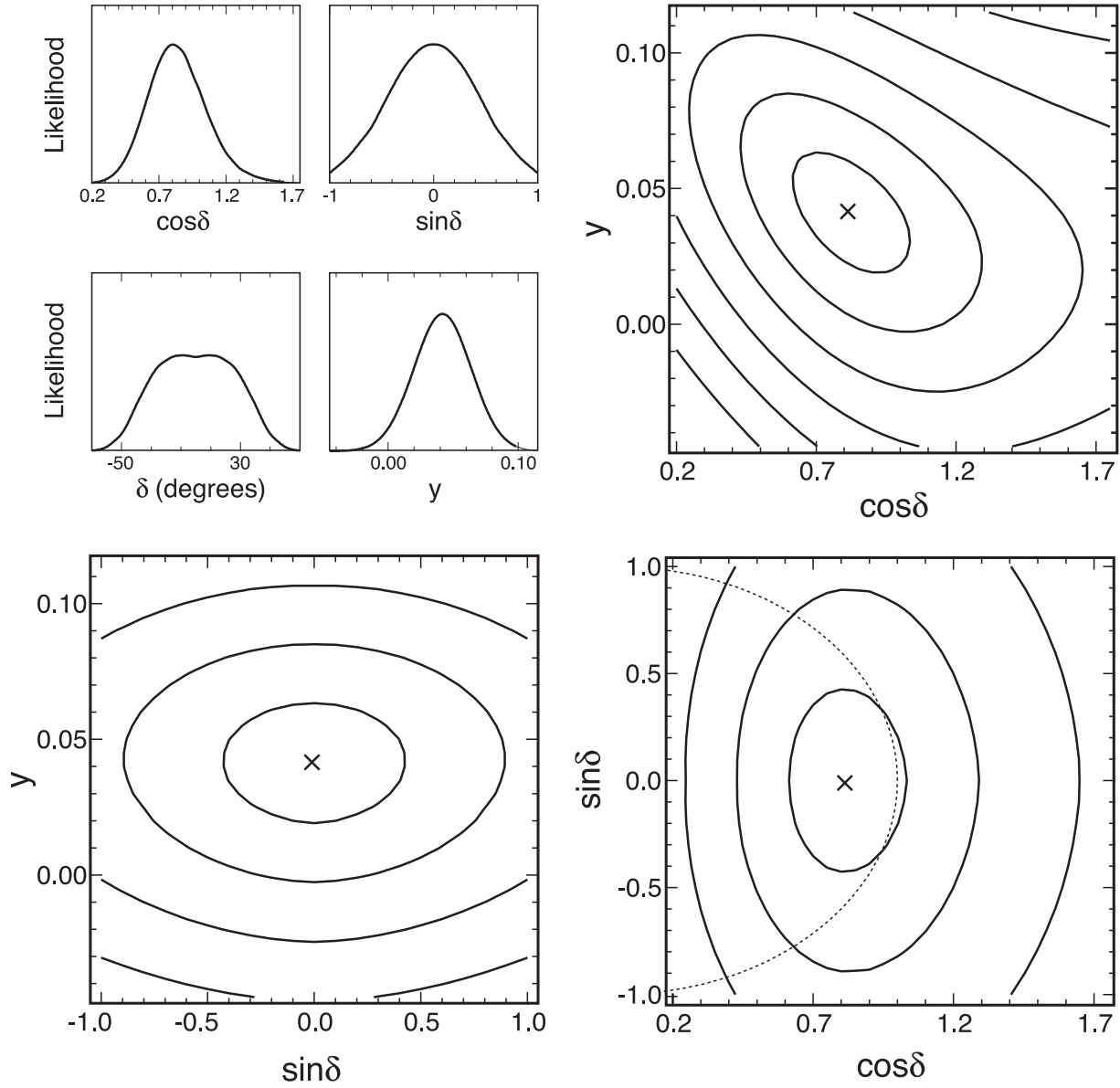


FIG. 9. Standard Fit likelihoods including both statistical and systematic uncertainties for $\cos \delta$, $\sin \delta$, δ , and y . The two-dimensional likelihoods are shown as contours in increments of 1σ , where $\sigma = \sqrt{\Delta\chi^2}$.

- [15] R. L. Kingsley, Phys. Lett. B **63**, 329 (1976).
- [16] M. Goldhaber and J. L. Rosner, Phys. Rev. D **15**, 1254 (1977).
- [17] I. I. Bigi and A. I. Sanda, Phys. Lett. B **171**, 320 (1986).
- [18] I. I. Bigi, SLAC-PUB-4000. *Invited talk given at Workshop on Physics Simulation at High Energies, Madison, WI, May 5-16, 1986.*
- [19] I. I. Bigi, UND-HEP-89-BIG01, also SLAC-R-343, pp. 169–195. *Given at Tau Charm Factory Workshop, Stanford, CA, May 23-27, 1989.*
- [20] Z. Z. Xing, Phys. Rev. D **55**, 196 (1997) [arXiv:hep-ph/9606422].

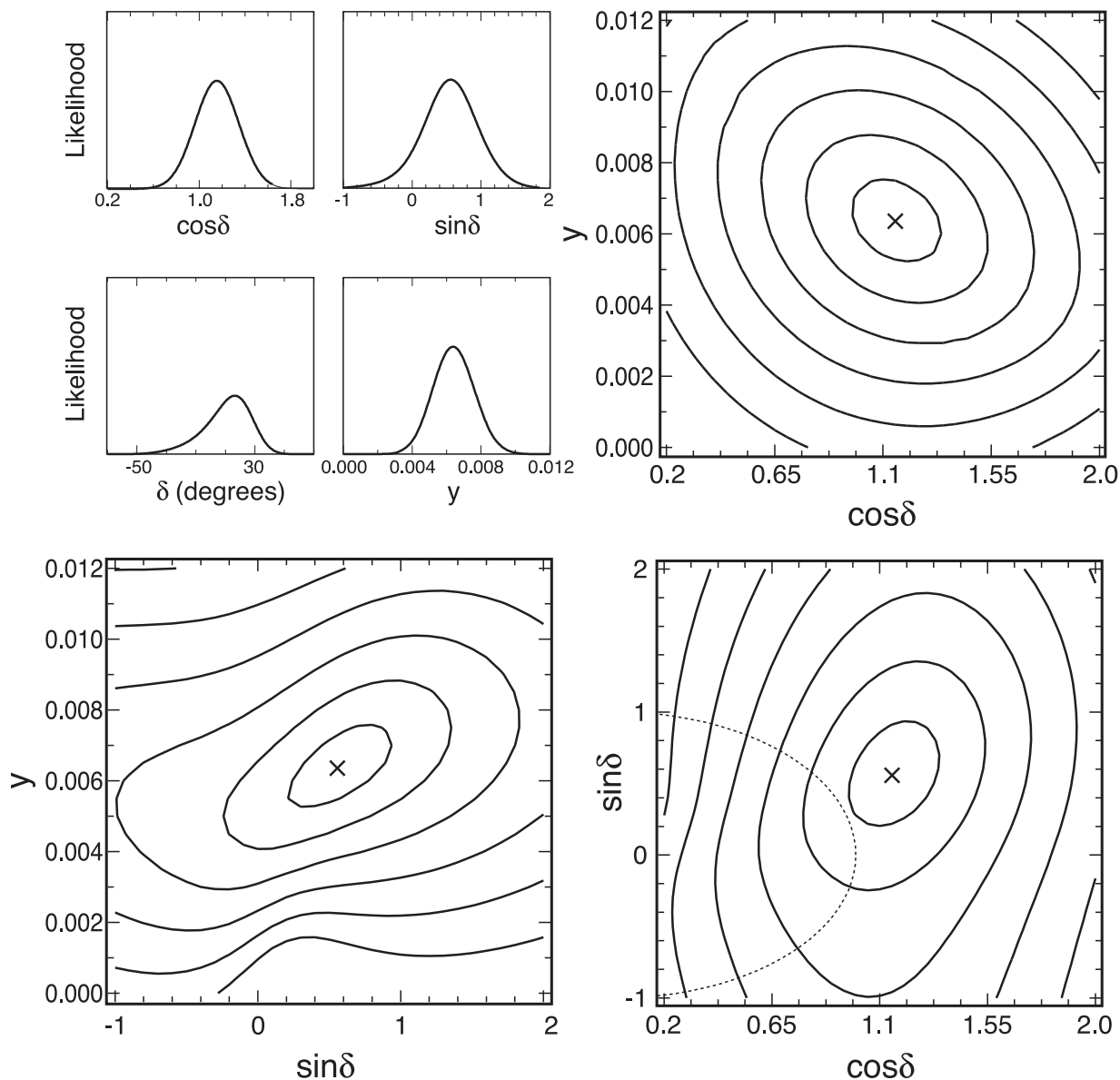


FIG. 10. Extended Fit likelihoods including both statistical and systematic uncertainties for $\cos \delta$, $\sin \delta$, δ , and y . The two-dimensional likelihoods are shown as contours in increments of 1σ , where $\sigma = \sqrt{\Delta\chi^2}$.

- [21] S. Bianco, F. L. Fabbri, D. Benson and I. Bigi, Riv. Nuovo Cim. **26N7**, 1 (2003) [arXiv:hep-ex/0309021].
- [22] D. Atwood and A. A. Petrov, Phys. Rev. D **71**, 054032 (2005) [arXiv:hep-ph/0207165].
- [23] D. M. Asner and W. M. Sun, Phys. Rev. D **73**, 034024 (2006) [Erratum-ibid. **77**, 019901(E) (2008)] [arXiv:hep-ph/0507238].
- [24] R. Aaij *et al.* [LHCb Collaboration], Phys. Rev. Lett. **108**, 111602 (2012) [arXiv:1112.0938 [hep-ex]].
- [25] T. Aaltonen *et al.* [CDF Collaboration], arXiv:1207.2158 [hep-ex].

- [26] T. Aaltonen *et al.* [CDF Collaboration], Phys. Rev. D **85**, 012009 (2012) [arXiv:1111.5023 [hep-ex]].
- [27] N. Neri, arXiv:1208.5877 [hep-ex].
- [28] D. Atwood and A. Soni, Phys. Rev. D **68**, 033003 (2003) [hep-ph/0304085].
- [29] R. A. Briere *et al.* [CLEO Collaboration], Phys. Rev. D **80**, 032002 (2009) [arXiv:0903.1681 [hep-ex]].
- [30] Y. Kubota *et al.*, Nucl. Instrum. Meth. A **320**, 66 (1992).
- [31] T. S. Hill, Nucl. Instrum. Meth. A **418**, 32 (1998).
- [32] D. Peterson *et al.*, Nucl. Instrum. Meth. A **478**, 142 (2002).
- [33] M. Artuso *et al.*, Nucl. Instrum. Meth. A **502**, 91 (2003);
- [34] R.A. Briere *et al.* [CLEO-c/CESR-c Taskforces & CLEO-c Collaboration], Cornell LEPP preprint CLNS 01/1742 (2001).
- [35] Computer code GEANT 3.21 in R. Brun *et al.*, CERN Report No. W5013 (unpublished).
- [36] H. Albrecht *et al.* [ARGUS Collaboration], Phys. Lett. B **241**, 278 (1990).
- [37] W. S. Brower and H. P. Paar, Nucl. Instrum. Meth. A **421**, 411 (1999) [hep-ex/9710029].
- [38] T. Hokuue *et al.* [Belle Collaboration], Phys. Lett. B **648**, 139 (2007) [hep-ex/0604024].
- [39] J. Beringer *et al.* [Particle Data Group], Phys. Rev. D **86**, 010001 (2012).
- [40] D. Asner *et al.* [Heavy Flavor Averaging Group Collaboration], arXiv:1010.1589 [hep-ex].
- [41] S. Dobbs *et al.* [CLEO Collaboration], Phys. Rev. D **76**, 112001 (2007) [arXiv:0709.3783 [hep-ex]].
- [42] D. Besson *et al.* [CLEO Collaboration], Phys. Rev. D **80**, 032005 (2009) [arXiv:0906.2983 [hep-ex]].
- [43] <http://www.aip.org/pubservs/epaps.html>.